Improved phase-field-based lattice Boltzmann method for thermocapillary flow

Liqing Yue,[1] Zhenhua Chai,[1,2,*] Huili Wang,[3] and Baochang Shi[1,2]

[1]*School of Mathematics and Statistics, Huazhong University of Science and Technology, Wuhan 430074, China*

[2]*Hubei Key Laboratory of Engineering Modeling and Scientific Computing, Huazhong University of Science and Technology, Wuhan 430074, China*

[3]*School of Mathematical and Computer Sciences, Wuhan Textile University, Wuhan 430074, China*

(Received 9 June 2021; accepted 6 January 2022; published 31 January 2022)

In this paper, we present an improved phase-field-based lattice Boltzmann (LB) method for thermocapillary flows with large density, viscosity, and thermal conductivity ratios. The present method uses three LB models to solve the conservative Allen-Cahn equation, the incompressible Navier-Stokes equations, and the temperature equation. To overcome the difficulty caused by the convection term in solving the convection-diffusion equation for the temperature field, we first rewrite the temperature equation as a diffuse equation where the convection term is regarded as the source term and then construct an improved LB model for the diffusion equation. The macroscopic governing equations can be recovered correctly from the present LB method; moreover, the present LB method is much simpler and more efficient. In order to test the accuracy of this LB method, several numerical examples are considered, including the planar thermal Poiseuille flow of two immiscible fluids, the two-phase thermocapillary flow in a nonuniformly heated channel, and the thermocapillary Marangoni flow of a deformable bubble. It is found that the numerical results obtained from the present LB method are consistent with the theoretical prediction and available numerical data, which indicates that the present LB method is an effective approach for the thermocapillary flows.

DOI: 10.1103/PhysRevE.105.015314

I. INTRODUCTION

Thermocapillary convection is the phenomenon of fluid movement induced by the difference in surface tension at a two-phase interface which is caused by a temperature gradient. For most cases, the surface tension is a decreasing function of the temperature, and bubbles or droplets in the low-temperature region with the large surface tension gradually move to the high-temperature region with the low surface tension due to induced thermocapillary stresses (also called Marangoni stresses [1]). Thermocapillary convection not only has a wide range of industrial applications [2–9], for example, crystal growth, coating, and thermocapillary-induced patterning of thin liquid films, but also plays an important role in many physical processes [10,11]. To explore the physical mechanism of thermocapillary flows, theoretical and experimental methods have been developed [12–17].

In addition to the two above types of research methods, numerical simulation has also been an important approach in the study of thermocapillary flows which involves multiple physical fields. For this complex multiphase problem, some numerical approaches have been developed, including the volume-of-fluid method [18,19], the front-tracking method [20,21], and the level-set method [22,23]. Ma and Bothe [24] used the volume-of-fluid method to study the thermocapillary Marangoni effect on the deformable droplet. Nas and Tryggvason [25] adopted the front-tracking method to investigate the thermocapillary interaction of two bubbles or drops and then Lu *et al.* [26] also applied the same method to simulate the thermocapillary interaction of a bubble with an obstruction. Balcázar *et al.* [27] introduced a novel multiple-marker level-set method for deformable bubbles and droplets, in which all physical properties are assumed to vary smoothly in a narrow band around the interface to avoid numerical instability; additionally, a new reinitialization equation was also considered in their work. We note that although all of these numerical methods are successful in the study of thermocapillary flows, they also have some defects. The volume-of-fluid method needs an extra reconstruction of the phase interface, while for the front-tracking method, the moving interface must be restructured and the transfer of information between the moving front and the fixed grid must be considered. Therefore, the volume-of-fluid method and the front-tracking method do not avoid explicit tracking of the dynamic interface in both mathematical formulation and numerical computation [28]. As for the level-set method, a reinitialization equation needs to be solved [27]. In addition, the three above methods also suffer from numerical instability at the interface region when the interfacial tension becomes a dominant factor [29]. In recent years, as an alternative, the phase-field method, which has a clear physical background and simple structure and is easy to implement numerically, has become a powerful and popular tool for thermocapillary flows without tracking the evolution of the phase interface [30]. In this method, an order parameter is introduced to characterize the different phases, and the range over which it changes is the thickness of the interface. Actually, there

*Corresponding author. hustczh@hust.edu.cn

are two popular kinds of mathematical models used to describe the interface: One is the fourth-order Cahn-Hilliard (CH) equation [31,32] and the other is the second-order Allen-Cahn (AC) equation [33–35]. Some researchers have used this method to investigate the interfacial dynamics with thermocapillary effects. For instance, Guo and Lin [36] first proposed a phase-field model for two-phase flows with the thermocapillary effect and then adopted a finite-difference scheme in time and a conformal finite-element method in space for the Navier-Stokes equations and the CH equation. Verschueren *et al.* [37] considered a phase-field model for the thermocapillary flow instability in the Hele-Shaw cell and applied the Galerkin-type spectral-element method to solve the governing equations.

In this work, we consider the mesoscopic lattice Boltzmann (LB) method for thermocapillary flows. The LB method, as a kinetic-based approach, has gained great success in the study of complex multiphase flows for its distinct features [38–44]. In this method, there are several multiphase LB models, including the pseudopotential LB model [45,46], the color gradient LB model [47], and the phase-field-based LB model [48,49]. These LB models also have been extended to simulate thermocapillary flows. Gupta *et al.* [50] adopted the pseudopotential LB model to study the influence of thermocapillarity on the breakup of fluid threads in a microfluidic T junction, but the pseudopotential LB method usually suffers from large spurious currents [51]. Liu *et al.* [52–56] used the LB method to conduct a series of studies on thermocapillarity flows, and these works can be divided into two categories: The first is one in which the governing equations of all physical fields are solved by the LB models [52–55] and the second is where the governing equations are solved by a hybrid approach in which the temperature equation is solved by the finite-difference method [56]. However, these works may also have some limitations. For the former, the LB models can only study thermocapillary flows with the same specific-heat capacities and densities of two fluids; in other words, the ratios of the specific-heat capacities and densities are assumed to be 1. For the latter, the CH-equation-based LB model proposed by Lee and Liu [57] is used to describe the interface, while this LB model may not preserve the total mass of a system and is non-Galilean invariant due to the discretization errors [56]. Also, the hybrid method may lead to inconsistency of computation, which makes it difficult to solve the problem with a complex boundary [56]. Similarly, Mitchell *et al.* [58] also used the hybrid method to investigate thermocapillary flows. In their work, the temperature equation was solved by a fourth-order Runge-Kutta algorithm; however, the phase-field equation could not be recovered correctly from the LB method through the Chapman-Enskog analysis [49]. Zheng *et al.* [59] constructed another LB method with continuous surface force to simulate the thermocapillary migration of a two-dimensional deformable droplet, but the CH equation could not be correctly recovered due to the existence of the fourth-order spatial derivative; additionally, the density ratio of the droplet and the ambient fluid was assumed to be unity [59]. Recently, Hu *et al.* [60] also established a new LB method for thermocapillary flow with a large density ratio, but the continuity equation and temperature equation could not be recovered correctly through the Chapman-Enskog analysis, which may have some influence on the accuracy of the LB model.

To overcome the drawbacks of some previous works, and based on the above-mentioned works [58,60,61], we present an improved LB method for thermocapillary flows with large density, viscosity, and thermal conductivity ratios. In this LB method, the second-order conservative AC equation is adopted to capture the interface since it possesses the potential in the volume preservation property, as well as good numerical stability in the simulations of the multiphase flow with a large density ratio, compared to the fourth-order CH equation [62]. In particular, an improved LB model is proposed for the diffusion equation for the temperature field, which is an equivalent version of the commonly used one. Through the Chapman-Enskog analysis, the governing equations for all physical fields can be recovered correctly from the present LB method. We also perform some numerical experiments to test the present LB method and find that the numerical results are in good agreement with the analytical solutions and some available numerical data. In addition, compared to some previous LB methods [59,60], the proposed LB method also works well for the Marangoni migration of the deformable bubble with large density, viscosity, and thermal conductivity ratios.

The rest of the paper is organized as follows. In Sec. II the LB method for thermocapillary flows is presented. In Sec. III we conduct some simulations to test the improved LB method. A summary and some conclusions are given in Sec. IV.

II. LATTICE BOLTZMANN METHOD FOR THERMOCAPILLARY FLOWS

A. LB model for the interface capturing equation

In the phase-field method, the kinetics and morphology evolution of phase separation is characterized by a phase-field equation for the order parameter ϕ. Compared to the fourth-order CH equation, the second-order conservative AC (CAC) equation is more efficient and less dispersive [49,63,64]. For this reason, the CAC equation is used to depict interface evolution [63]

$$\partial_t \phi + \nabla \cdot (\phi \mathbf{u}) = \nabla \cdot (M_\phi \nabla \phi) - \nabla \cdot \left(M_\phi \frac{\nabla \phi}{|\nabla \phi|} \frac{1-\phi^2}{\sqrt{2}D} \right), \tag{1}$$

where the order parameter ϕ changes from -1 to 1. Here $\phi_1 = 1$ and $\phi_2 = -1$ represent the different phases; the interface between two phases is marked by the contour level of $\phi = 0$. In addition, $\mathbf{u} = (u_x, u_y)$ is the fluid velocity, M_ϕ is the mobility, and D is the thickness of diffuse interface. At the equilibrium state, the distribution of the order parameter can be given by

$$\phi(x) = \tanh\left(\frac{x}{\sqrt{2}D} \right), \tag{2}$$

where x is the distance to the interface.

In the present LB model for the CAC equation, the evolution equation with the single-relaxation-time collision

operator reads [49,65]

$$f_k(\mathbf{x}+\mathbf{c}_k\Delta t, t+\Delta t) = f_k(\mathbf{x},t) - \frac{1}{\tau_f}[f_k(\mathbf{x},t) - f_k^{\mathrm{eq}}(\mathbf{x},t)] + \Delta t\left(1-\frac{1}{2\tau_f}\right)F_k(\mathbf{x},t), \quad k=0,\ldots,q-1, \tag{3}$$

where $f_k(\mathbf{x},t)$ is the distribution function with velocity $\mathbf{c}_k$ at position $\mathbf{x}$ and time t, τ_f is the dimensionless relaxation time, Δt is the time step, and $F_k(\mathbf{x},t)$ is the discrete source term. In addition, f_k^{eq} is the equilibrium distribution function and is given by [49]

$$f_k^{\mathrm{eq}} = \omega_k\phi\left(1+\frac{\mathbf{c}_k\cdot\mathbf{u}}{c_s^2}\right), \tag{4}$$

where $\{\omega_k, k=0,\ldots,q-1\}$ are the weight coefficients which are dependent on the specified lattice model, $\mathbf{c}_k = c\mathbf{e}_k$ is the discrete velocity with the lattice speed $c=\Delta x/\Delta t$ (Δx is the lattice spacing) and the direction vector $\mathbf{e}_k$, and c_s is the lattice sound speed that is related to lattice speed c. In our simulations, the lattice speed c, Δx, and Δt are set to 1. For the two-dimensional problems considered here, the two-dimensional nine-velocity (D2Q9) lattice model is adopted for the CAC equation, and in this model, the discrete velocity, weighting coefficient, and sound speed are given, respectively, by

$$\mathbf{c}_k = c\mathbf{e}_k = c\begin{bmatrix}0 & 1 & 0 & -1 & 0 & 1 & -1 & -1 & 1\\ 0 & 0 & 1 & 0 & -1 & 1 & 1 & -1 & -1\end{bmatrix}, \tag{5a}$$

$$\omega_k = \begin{cases}\omega_0 = \frac{4}{9},\\ \omega_{1-4} = \frac{1}{9},\\ \omega_{5-8} = \frac{1}{36},\end{cases} \tag{5b}$$

$$c_s^2 = \frac{c^2}{3}. \tag{5c}$$

To recover the CAC equation correctly, the source term F_k in Eq. (3) should be defined as [49]

$$F_k = \frac{\omega_k\mathbf{c}_k\cdot\left[\partial_t(\phi\mathbf{u}) + c_s^2\left(M_\phi\frac{\nabla\phi}{|\nabla\phi|}\frac{1-\phi^2}{\sqrt{2}D}\right)\right]}{c_s^2}, \tag{6}$$

where the time derivative term $\partial_t(\phi\mathbf{u})$ is included in order to eliminate some additional terms in the recovered equation [49,64,66]. The order parameter in the present LB model can be calculated as

$$\phi = \sum_k f_k. \tag{7}$$

Physically, the distribution of the fluid density ρ for the two phases is consistent with that of the order parameter ϕ. To satisfy this condition, the expression of density should be a function of the order parameter and is given as

$$\rho = \frac{\rho_1-\rho_2}{\phi_1-\phi_2}(\phi-\phi_2)+\rho_2. \tag{8}$$

Through the Chapman-Enskog analysis, the CAC equation can be recovered correctly from the LB equation (3) with the following mobility [49]:

$$M_\phi = c_s^2(\tau_f - 0.5)\Delta t. \tag{9}$$

In addition, the derivative terms in the LB model must be discretized with some suitable difference schemes. For simplicity, the explicit Euler scheme is used to compute the temporal derivative in Eq. (6). In contrast, to keep the collision process implemented locally, the gradient term $\nabla\phi$ can be calculated by the nonequilibrium distribution function [49,64,67], and after some algebraic manipulations, the local scheme for the gradient term $\nabla\phi$ can be given by [49]

$$|\nabla\phi| = \frac{-|C|-B}{A}, \tag{10}$$

$$\nabla\phi = \frac{C}{A+\frac{B}{|\nabla\phi|}}, \tag{11}$$

where

$$A = -c_s^2\tau_f\Delta t, \tag{12a}$$

$$B = M_\phi\frac{1-\phi^2}{\sqrt{2}D}, \tag{12b}$$

$$C = \sum_k \mathbf{c}_k\left(f_k - f_k^{\mathrm{eq}}\right) + \frac{\Delta t}{2}\partial_t(\phi\mathbf{u}). \tag{12c}$$

B. LB model for the Navier-Stokes equations

In this work, we consider the incompressible Navier-Stokes equations for the fluid flows [64,68]

$$\nabla\cdot\mathbf{u} = 0, \tag{13a}$$

$$\partial_t(\rho\mathbf{u}) + \nabla\cdot(\rho\mathbf{u}\mathbf{u}) = -\nabla p + \nabla\cdot\mu(\nabla\mathbf{u}+\nabla\mathbf{u}^T) + \mathbf{G} + \mathbf{F}_s, \tag{13b}$$

where p is the hydrodynamic pressure, μ is dynamic viscosity ($\mu=\rho\nu$, with ν the kinematic viscosity), $\mathbf{F}_s$ is the interface force, and $\mathbf{G}$ is the body force. For the thermocapillary flows, the interface force can be expressed as [56]

$$\mathbf{F}_s = (-\sigma\lambda\mathbf{n} + \nabla_s\sigma)\delta, \tag{14}$$

where σ is the surface tension, $\lambda = \nabla\cdot\mathbf{n}$ is the interface curvature, $\mathbf{n} = \frac{\nabla\phi}{|\nabla\phi|}$ is the unit normal vector, $\nabla_s = (I-\mathbf{n}\otimes\mathbf{n})\cdot\nabla$ is the surface gradient operator, and $\delta = \gamma|\nabla\phi|^2$ is the Dirac delta function and satisfies the condition

$$\gamma\int_{-\infty}^{\infty}\delta\,dx = 1. \tag{15}$$

Based on previous work [48], we can obtain the expression of the parameter γ,

$$\gamma = \frac{6\sqrt{\lambda}}{\sqrt{2\beta}\left(\phi_1^3-\phi_2^3\right)}, \tag{16}$$

where β is a parameter. With the aid of Eq. (16), we can further derive the interface force $\mathbf{F}_s$,

$$\mathbf{F}_s = \frac{3\sqrt{2}}{4}D\left(|\nabla\phi|^2\nabla\sigma - (\nabla\sigma\cdot\nabla\phi)\nabla\phi + \frac{\sigma}{D^2}\mu\nabla\phi\right), \tag{17}$$

where $\mu = (\phi-\phi_1)(\phi-\phi_2)(\phi-\frac{\phi_1+\phi_2}{2}) - D^2\nabla^2\phi$ is the chemical potential, in which the Laplace operator can be

calculated as

$$\nabla^2\phi = \sum_{k\neq 0} \frac{2\omega_k[\phi(\mathbf{x}+\mathbf{c}_k\Delta t)-\phi(\mathbf{x})]}{{c_s}^2\Delta t^2}. \tag{18}$$

For the thermocapillary flows, the equation of state is used to describe the relation between the surface tension σ and temperature T,

$$\sigma(T) = \sigma_{\rm ref} - \sigma_T(T - T_{\rm ref}), \tag{19}$$

where $T_{\rm ref}$ is the reference temperature and $\sigma_T = \frac{\partial\sigma}{\partial T}$ is the rate of surface tension with the temperature.

Similarly, the evolution equation of the LB model for the Navier-Stokes equations can be written as [68,69]

$$\begin{aligned} g_k(\mathbf{x}+\mathbf{c}_k\Delta t, t+\Delta t) = g_k(\mathbf{x},t) - \frac{1}{\tau_g}\left[g_k(\mathbf{x},t) - g_k^{\rm eq}(\mathbf{x},t)\right] \\ + \Delta t\left(1-\frac{1}{2\tau_g}\right)G_k(\mathbf{x},t), \\ k = 0,\ldots,q-1, \end{aligned} \tag{20}$$

where $g_k(\mathbf{x},t)$ is the distribution function of the LB model for the flow field, $g_k^{\rm eq}$ is the equilibrium distribution function, τ_g is the relaxation time related to the kinematic viscosity ν, and $\mathbf{G}_k(\mathbf{x},t)$ is the discrete force term. To recover the incompressible Navier-Stokes equations correctly, $g_k^{\rm eq}$ should be designed as [68]

$$g_k^{\rm eq} = \begin{cases} \frac{p}{c_s^2}(\omega_k - 1) + \rho s_k(\mathbf{u}), & k = 0 \\ \frac{p}{c_s^2}\omega_k + \rho s_k(\mathbf{u}), & k \neq 0, \end{cases} \tag{21}$$

with

$$s_k(\mathbf{u}) = \omega_k\left[\frac{\mathbf{c}_k\cdot\mathbf{u}}{c_s^2} + \frac{(\mathbf{c}_k\cdot\mathbf{u})^2}{2c_s^4} - \frac{\mathbf{u}\cdot\mathbf{u}}{2c_s^2}\right]. \tag{22}$$

The discrete force term is given by [68]

$$\begin{aligned} \mathbf{G}_k = \omega_k\Bigg[\mathbf{u}\cdot\nabla\rho \\ + \frac{\mathbf{c}_k\cdot\mathbf{F}_s}{c_s^2} + \frac{\left(\mathbf{c}_k\mathbf{c}_k - c_s^2\mathbf{I}\right):\left(\mathbf{u}\tilde{\mathbf{F}}+\tilde{\mathbf{F}}\mathbf{u}\right):\left(\mathbf{c}_k\mathbf{c}_k - c_s^2\mathbf{I}\right)}{2c_s^4}\Bigg], \end{aligned} \tag{23}$$

where $\tilde{\mathbf{F}} = \mathbf{F}_s + \nabla(\rho c_s^2)$ and the gradient term $\nabla\phi$ in $\mathbf{F}_s$ in the collision step can be calculated locally by Eq. (11). For the Navier-Stokes equations, the D2Q9 lattice model described previously is also adopted. Through the Chapman-Enskog analysis, the present LB model can correctly recover Eq. (13) with the kinematic viscosity

$$\nu = c_s^2(\tau_g - 0.5)\Delta t. \tag{24}$$

Additionally, the macroscopic velocity and pressure are calculated as

$$\mathbf{u} = \frac{1}{\rho}\left(\sum_k \mathbf{c}_k g_k + \frac{\Delta t}{2}\mathbf{F}_s\right), \tag{25}$$

$$p = \frac{c_s^2}{1-\omega_0}\left[\sum_{k\neq 0} g_k + \frac{\Delta t}{2}\mathbf{u}\cdot\nabla\rho + \rho s_0(\mathbf{u})\right]. \tag{26}$$

It should be noted that in Eq. (25), the gradient term $\nabla\phi$ in $\mathbf{F}_s$ must be calculated. Although the local scheme [Eq. (11)] can be adopted, we need to solve the nonlinear equation (25) to obtain the velocity. To overcome the problem, as in previous works [70,71], the gradient term in Eq. (25) is computed by the second-order isotropic central-difference scheme

$$\nabla\phi = \sum_{k\neq 0}\frac{\omega_k\mathbf{c}_k\phi(\mathbf{x}+\mathbf{c}_k\Delta t)}{c_s^2\Delta t}. \tag{27}$$

C. LB model for the temperature equation

The following convection-diffusion equation is applied to describe the temperature field:

$$\rho C_p(\partial_t T + \mathbf{u}\cdot\nabla T) = \nabla\cdot(\kappa\nabla T). \tag{28}$$

Here T is the temperature, C_p is the specific-heat capacity, and κ is the thermal conductivity. As stated previously, in some available LB methods for thermocapillary flows, the density ρ and specific-heat capacity C_p of the two fluids are assumed to be the same as each other; however, this is not consistent with most of the problems in practice. On the other hand, when the traditional numerical method is applied to solve Eq. (28), the mass conservation of system may not be ensured [56,72]. In the following, we will develop an alternative LB model for the temperature equation. To this end, we first rewrite Eq. (28) in another form where the convection term is regarded as part of the source term [58,61],

$$\partial_t T = \nabla\cdot(\alpha\nabla T) + R_1, \tag{29}$$

where

$$R_1 = -\mathbf{u}\cdot\nabla T - \kappa\nabla T\cdot\nabla\left(\frac{1}{\rho C_p}\right) \tag{30}$$

is the source term and $\alpha = \kappa/\rho C_p$ is the thermal diffusivity. It should be noted that in the phase-field theory, the physical parameter ψ (e.g., the thermal conductivity) can be expressed as a linear function of the order parameter [60,73],

$$\psi = \frac{\psi_1 - \psi_2}{\phi_1 - \phi_2}(\phi - \phi_2) + \psi_2. \tag{31}$$

According to Eq. (31), the specific-heat capacity and thermal conductivity can be given by [60].

$$C_p = \frac{C_{p_1} - C_{p_2}}{\phi_1 - \phi_2}(\phi - \phi_2) + C_{p_2}, \tag{32}$$

$$\kappa = \frac{\kappa_1 - \kappa_2}{\phi_1 - \phi_2}(\phi - \phi_2) + \kappa_2, \tag{33}$$

which change continuously in the whole domain. Substituting Eqs. (8) and (32) in Eq. (30) yields another form of the source term

$$\begin{aligned} R_1 = -\mathbf{u}\cdot\nabla T - \kappa\nabla T \\ \cdot\left(-\frac{\rho(C_{p_1} - C_{p_2}) + C_p(\rho_1 - \rho_2)}{(\rho C_p)^2(\phi_1 - \phi_2)}\right)\nabla\phi. \end{aligned} \tag{34}$$

We now present a simple LB model for the temperature equation (29). In this model, the evolution equation

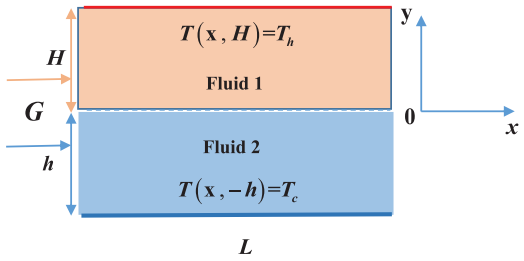

FIG. 1. Schematic of the thermocapillary flows with two immiscible fluids in a two-dimensional channel.

reads

$$h_k(\mathbf{x}+\mathbf{c}_k\Delta t, t+\Delta t) = h_k(\mathbf{x},t) - \frac{1}{\tau_h}\left[h_k(\mathbf{x},t) - h_k^{\mathrm{eq}}(\mathbf{x},t)\right] + \Delta t\left(1-\frac{1}{2\tau_h}\right)H_k(\mathbf{x},t), \quad k=0,\ldots,q-1, \tag{35}$$

where $h_k(\mathbf{x},t)$ is the distribution function for the temperature field, τ_h is the relaxation time corresponding to the thermal diffusivity, $H_k(\mathbf{x},t)=\omega_k R_1$ is the discrete source term related to R_1 in Eq. (34), and h_k^{eq} is the equilibrium distribution function and is defined as

$$h_k^{\mathrm{eq}} = \omega_k T. \tag{36}$$

The temperature T is computed as

$$T = \sum_k h_k + \frac{\Delta t}{2}R_1. \tag{37}$$

In Eq. (37) the gradient term $\nabla\phi$ in the source term R_1 is calculated by Eq. (27).

Based on the expressions of the equilibrium distribution function h_k^{eq} and discrete source term H_k, we can obtain the relations

$$\sum_k h_k^{\mathrm{eq}} = T, \quad \sum_k \mathbf{c}_k h_k^{\mathrm{eq}} = \mathbf{0}, \quad \sum_k \mathbf{c}_k\mathbf{c}_k h_k^{\mathrm{eq}} = c_s^2 T\mathbf{I}, \tag{38a}$$

$$\sum_k H_k = R_1, \quad \sum_k \mathbf{c}_k H_k = \mathbf{0}, \quad \sum_k \mathbf{c}_k\mathbf{c}_k H_k = c_s^2 R_1\mathbf{I}. \tag{38b}$$

Through the Chapman-Enskog analysis (see the Appendix for details), the temperature equation (29) can be recovered correctly from the present LB model with the thermal diffusivity $\alpha = \kappa/\rho C_p = c_s^2(\tau_h - \frac{1}{2})\Delta t$. We also note that in the present LB model for the temperature equation, the gradient term ∇T can be calculated locally,

$$\nabla T = -\frac{1}{\tau_h c_s^2 \Delta t}\sum_k \mathbf{c}_k\left(h_k - h_k^{\mathrm{eq}}\right). \tag{39}$$

With the help of Eqs. (11) and (39), the collision process of Eq. (35) can be implemented locally.

III. NUMERICAL RESULTS AND DISCUSSION

In this section, we consider three problems to test the present LB method and conduct a comparison of the present numerical results with analytical solutions and available data. The first one is the planar thermal Poiseuille flow of two immiscible fluids, the second one is two-phase thermocapillary flow in a nonuniformly heated channel, and the last one is the thermocapillary migration of a deformable bubble. For these problems, several important dimensionless parameters are first defined, including the Reynolds number Re, the Marangoni number Ma, the capillary number Ca, the fluid

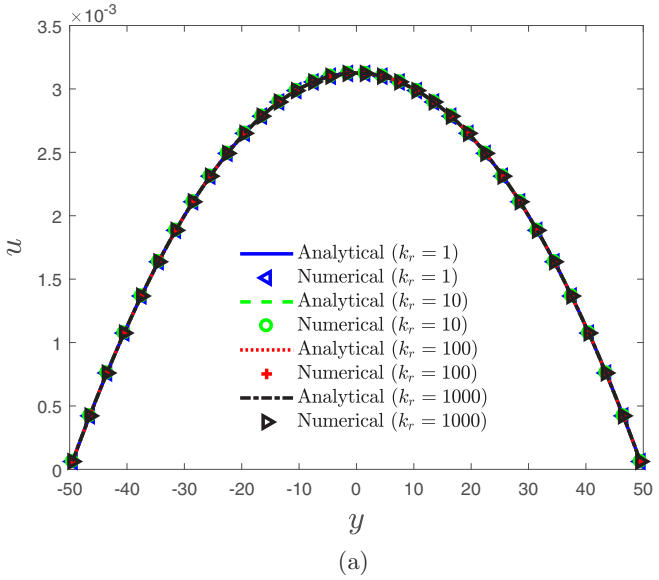

(a)

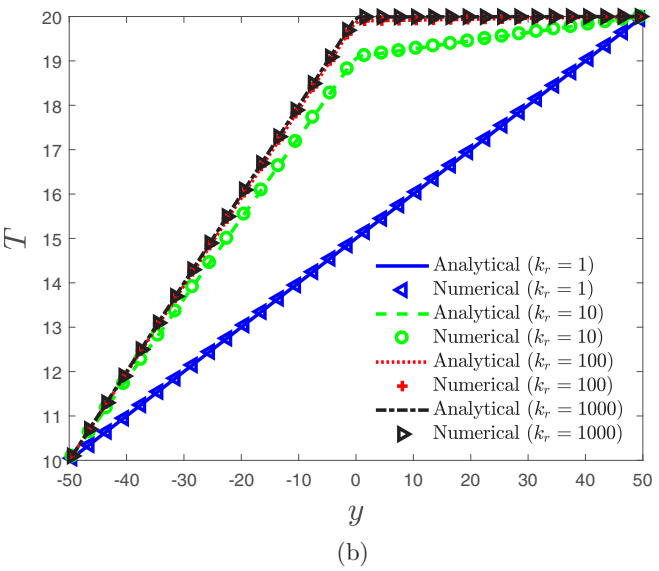

(b)

FIG. 2. Profiles of velocity (a) and temperature (b) along the vertical central line for $\nu_1=\nu_2=0.2$, $\rho_1=\rho_2=1.0$, $C_{p_1}=C_{p_2}=1$, and $\kappa_r=1$, 10, 100, and 1000.

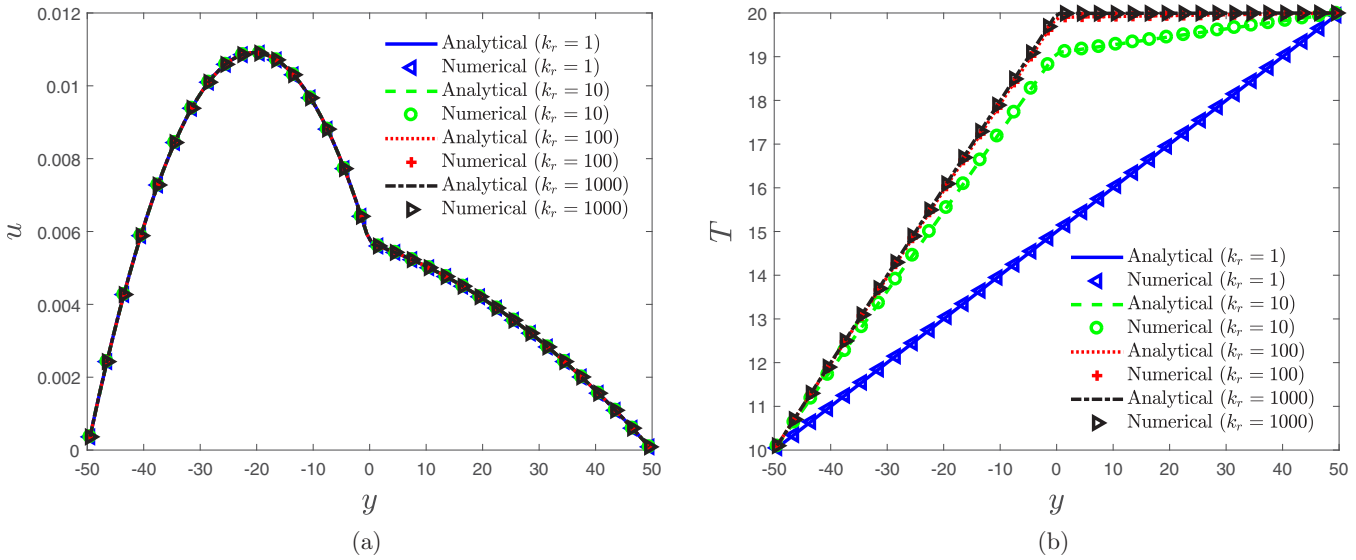

FIG. 3. Profiles of velocity (a) and temperature (b) along the vertical central line for $\nu_r = 0.1$, $\rho_1 = \rho_2 = 1.0$, $C_{p_1} = C_{p_2} = 1$, and $\kappa_r = 1$, 10, 100, and 1000.

density ratio ρ_r, the viscosity ratio μ_r, the thermal conductivity ratio κ_r, and the specific-heat capacity ratio C_{p_r}, as [56]

$$\mathrm{Re} = \frac{LU}{\nu_2}, \quad \mathrm{Ma} = \frac{\rho_2 C_{p_2} LU}{\kappa_2}, \quad \mathrm{Ca} = \frac{U\mu_2}{\sigma_{\mathrm{ref}}}, \tag{40}$$

$$\rho_r = \frac{\rho_2}{\rho_1}, \quad \mu_r = \frac{\mu_2}{\mu_1}, \quad \kappa_r = \frac{\kappa_2}{\kappa_1}, \quad C_{p_r} = \frac{C_{p_2}}{C_{p_1}}, \tag{41}$$

where the subscripts represent different phases.

For convenience, the mobility M_ϕ is set equal to 0.01. For the gradient term of the order parameter in the collision step, the local scheme is applied to ensure that the collision process is implement locally [Eq. (10)], while a second-order isotropic difference scheme [Eq. (27)] is employed in the computation of macroscopic variables [Eqs. (25) and (37)]. In addition, the gravity effect is neglected.

A. Planar thermal Poiseuille flow in a two-dimensional channel

We first consider the simple problem in Fig. 1, where the surface tension coefficient σ is fixed as a constant, the planar thermal flow is driven by an external force $\mathbf{G}$, and $H + h$ and L are the height and length of the channel. For this problem, we can obtain the analytical solutions of temperature and velocity [59],

$$T(y) = \begin{cases} \frac{\kappa_2(T_h - T_c)}{\kappa_1 H + \kappa_2 h} y + \frac{\kappa_1 H T_c + \kappa_2 h T_h}{\kappa_1 H + \kappa_2 h}, & -h \leqslant y \leqslant 0 \\ \frac{\kappa_1(T_h - T_c)}{\kappa_1 H + \kappa_2 h} y + \frac{\kappa_1 H T_c + \kappa_2 h T_h}{\kappa_1 H + \kappa_2 h}, & 0 \leqslant y \leqslant H, \end{cases} \tag{42}$$

$$u(y) = \begin{cases} \frac{\rho G_x h^2}{2\mu_1}\left[-\left(\frac{y}{h}\right)^2 + \left(\frac{H^2/h^2\mu_1 - \mu_2}{H/h\mu_1 + \mu_2}\right)\frac{y}{h} + \frac{(1+H/h)H\mu_1}{\mu_1 H + \mu_2 h}\right], & -h \leqslant y \leqslant 0 \\ \frac{\rho G_x H^2}{2\mu_2}\left[-\left(\frac{y}{H}\right)^2 + \left(\frac{\mu_1 - h^2/H^2\mu_2}{h/H\mu_2 + \mu_1}\right)\frac{y}{H} + \frac{(1+h/H)h\mu_2}{\mu_1 H + \mu_2 h}\right], & 0 \leqslant y \leqslant H. \end{cases} \tag{43}$$

The fluids in the different regions have different physical properties and they interact with each other only through the interface at $y = 0$. The top and bottom walls are stationary and kept at the constant temperatures T_h and T_c and the periodic boundary condition is adopted for the left and right boundaries for all physical fields. Here μ_i $(i = 1, 2)$ is the dynamic viscosity of the fluid. In order to test the accuracy of the present LB method, we conduct some numerical simulations at different ratios of thermal conductivity κ_r and set the other parameters as $\rho_1 = \rho_2 = 1$, $C_{p_1} = C_{p_2} = 1$, $\nu_1 = \nu_2 = 0.2$, $H = h = 50\Delta x$, $L = 10\Delta x$, $T_h = 20$, $T_c = 10$, $\mathbf{G} = (5 \times 10^{-7}, 0)$, and $D = 2$. In our simulations, the antibounceback scheme [74–76] is used for the Dirichlet boundary conditions of the temperature field, while the halfway bounceback scheme is adopted for the nonslip boundary condition of the flow field and the no-flux boundary condition of the phase field [77,78]. Based on the results shown in Fig. 2, it is found that the numerical results of velocity and temperature at different values of the thermal conductivity ratio ($\kappa_r = 1$, 10, 100, and 1000) are in good agreement with the analytical solutions. We further perform some numerical tests at different ratios of viscosity coefficient ν_r and plot the results in Figs. 3–5. From these figures we can observe that although the viscosity ratio has a great influence on the velocity field, it does not affect the temperature field, which is consistent with the analytic solution (42). Additionally, we also find that the present LB method works well for the thermal flows in the two-dimensional channel, even with the large ratios of thermal conductivity and viscosity.

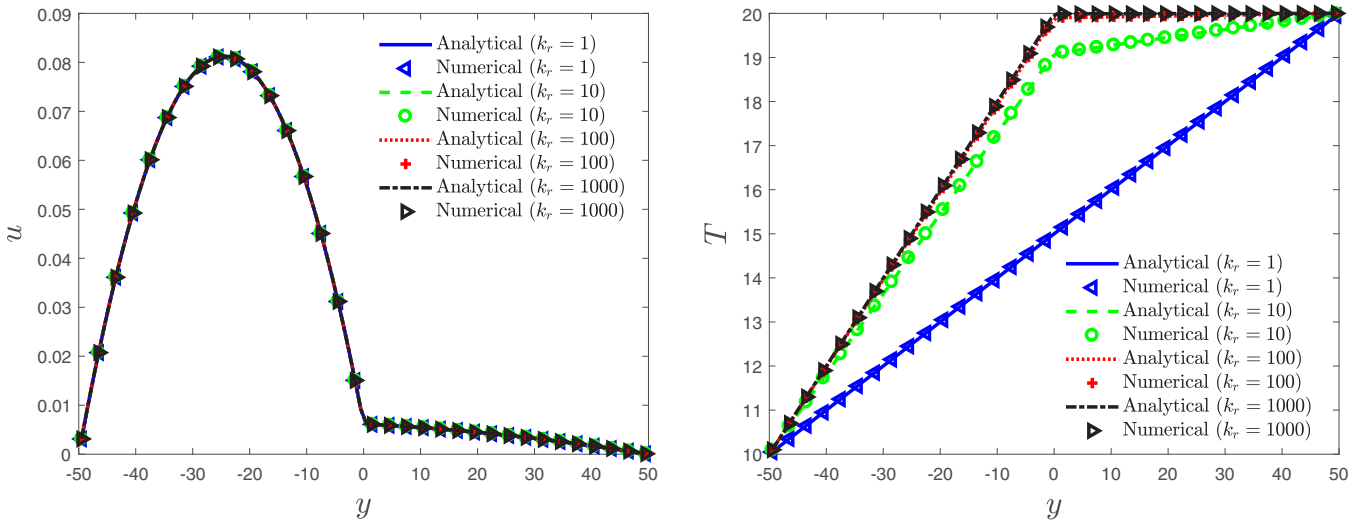

FIG. 4. Profiles of velocity (a) and temperature (b) along the vertical central line for $\nu_r = 0.01$, $\rho_1 = \rho_2 = 1.0$, $C_{p_1} = C_{p_2} = 1$, and $\kappa_r = 1$, 10, 100, and 1000.

B. Two-phase thermocapillary flow in a nonuniformly heated channel

In the second example, we consider the thermocapillary flow driven by the temperature gradient instead of the external force considered in the first problem, which is more complicated since the surface tension changes with temperature [see Eq. (19)]. For this problem, shown in Fig. 6, we impose a uniform temperature on the top wall and a sinusoidal temperature profile on the bottom wall,

$$T(x, H) = T_c, \tag{44}$$

$$T(x, -h) = T_h + T_0 \cos(\omega x), \tag{45}$$

where $T_0 < T_c < T_h$ and $\omega = 2\pi/L$ is a wave number, with L the length of the channel. Under the condition of $\mathrm{Re} \ll 1$, $\mathrm{Ma} \ll 1$, and $\mathrm{Ca} \ll 1$, we can obtain the analytic solutions of this problem [15]. For fluid 1,

$$T_A(x, y) = \frac{(T_h - T_c)y + \kappa_r T_c h + T_h H}{H + \kappa_r h} + T_0 t(\hat{H}, \hat{h}, \kappa_r) \sinh(\hat{H} - \omega y) \cos(\omega x), \tag{46}$$

$$U_x^A(x, y) = U_{\max}\left\{\left[A_1^H + \omega\left(A_2^H + A_3^H y\right)\right]\cosh(\omega y) + \left(A_3^H + \omega A_1^H y\right)\sinh(\omega y)\right\}\sin(\omega x), \tag{47}$$

$$U_y^A(x, y) = -\omega U_{\max}\left[A_1^H \cosh(\omega y) + \left(A_2^H + A_3^H y\right)\right]\sinh(\omega x), \tag{48}$$

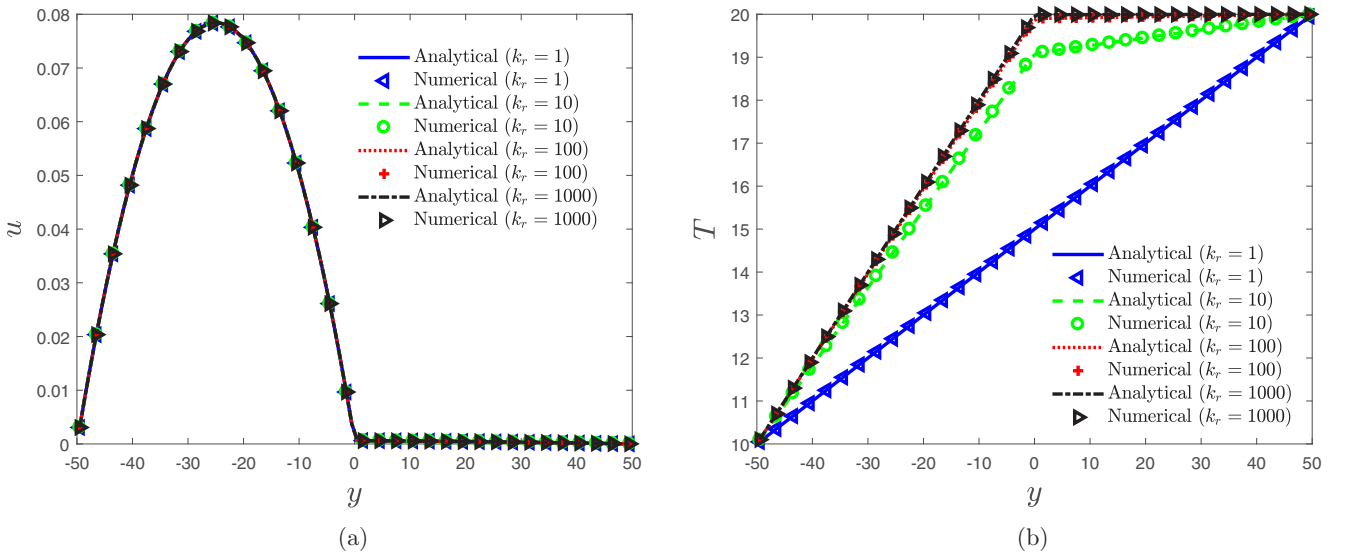

FIG. 5. Profiles of velocity (a) and temperature (b) along the vertical central line for $\nu_r = 0.001$, $\rho_1 = \rho_2 = 1.0$, $C_{p_1} = C_{p_2} = 1$, and $\kappa_r = 1$, 10, 100, and 1000.

and for fluid 2,

$$T_A(x,y) = \frac{\kappa(T_h - T_c)y + \kappa_r T_c h + T_h H}{H + \kappa_r h} + T_0 t(\hat{H},\hat{h},\kappa_r)[\sinh(\hat{H})\cos(\omega x) - \kappa_r \sinh(\omega y)\cosh(\hat{H})]\cos(\omega x), \tag{49}$$

$$U_x^A(x,y) = U_{\max}\left[A_1^h + \omega\left(A_2^h + A_3^h y\right)\right]\cosh(\omega y) + \left(A_3^h + \omega A_1^h y\right)\sinh(\omega y)\sin(\omega x), \tag{50}$$

$$U_y^A(x,y) = -\omega U_{\max}\left[A_1^h \cosh(\omega y) + \left(A_2^h + A_3^h y\right)\right]\sinh(\omega x). \tag{51}$$

The parameters appearing in these equations are defined as

$$\hat{H} = H\omega, \quad \hat{h} = h\omega, \tag{52}$$

$$t(\hat{H},\hat{h},\kappa_r) = [\kappa_r \sinh(\hat{h})\cosh(\hat{H}) + \sinh(\hat{H})\cosh(\hat{h})]^{-1}, \tag{53}$$

$$A_1^H = \frac{\sinh^2(\hat{H})}{\sinh^2(\hat{H}) - \hat{H}^2}, \quad A_2^H = \frac{-H\hat{H}}{\sinh^2(\hat{H}) - \hat{H}^2}, \quad A_3^H = \frac{2\hat{H} - \sinh(2\hat{H})}{2[\sinh^2(\hat{H}) - \hat{H}^2]}, \tag{54}$$

$$A_1^h = \frac{\sinh^2(\hat{h})}{\sinh^2(\hat{h}) - \hat{h}^2}, \quad A_2^h = \frac{-h\hat{h}}{\sinh^2(\hat{h}) - \hat{h}^2}, \quad A_3^h = \frac{\sinh(2\hat{h}) - 2\hat{h}}{2[\sinh^2(\hat{h}) - \hat{h}^2]}, \tag{55}$$

$$U_{\max} = -\frac{T_0\sigma_T}{\eta_2} a(\hat{H},\hat{h},\kappa_r)s(\hat{H},\hat{h},\kappa_r), \tag{56}$$

where

$$a(\hat{H},\hat{h},\kappa_r) = \sinh(\hat{H})t(\hat{H},\hat{h},\kappa_r), \tag{57}$$

$$s(\hat{H},\hat{h},\kappa_r) = \frac{[\sinh^2(\hat{H}) - \hat{H}^2][\sinh^2(\hat{h}) - \hat{h}^2]}{\nu_r[\sinh^2(\hat{h}) - \hat{h}^2][\sinh(2\hat{H}) - 2\hat{H}] + [\sinh^2(\hat{H}) - \hat{H}^2][\sinh(2\hat{h}) - 2\hat{h}]}. \tag{58}$$

In our simulations, the channel length is $L = 160\Delta x$, $H = h = 40\Delta x$, $T_c = 10$, $T_h = 20$, $T_0 = 4$, $\sigma_T = 5 \times 10^{-4}$, $\sigma_{\text{ref}} = 2.5 \times 10^{-2}$, $\nu_1 = \nu_2 = 0.2$, $\rho_1 = \rho_2 = 1$, and $C_{p_1} = C_{p_2} = 1$. These values can result in the typical values of Re, Ma, and Ca at $O(0.01)$ or at most $O(0.1)$. To study the influence of the thermal conductivity ratio κ_r on the distributions of velocity and temperature, we conduct some simulations with $\kappa_r = 0.1$, 0.2, and 1 and present the contours of the temperature in Fig. 7. As seen from this figure, the numerical results (solid line) are consistent with the analytical solutions (dashed line) given by Eqs. (46) and (49). However, it should be noted that the numerical results slightly deviate from the analytical solutions near the interface for the cases of $\kappa_r = 0.1$ and 0.2, which is mainly caused by the finite thickness of the interface in the phase-field LB method. To quantitatively evaluate the accuracy of the present LB method and compare with some previous LB models, the relative error is considered,

$$\text{Err}_\psi = \frac{\sum_j |\psi(x_j,t) - \psi^*(x_j,t)|}{\sum_j |\psi^*(x_j,t)|}, \tag{59}$$

where ψ and ψ^* are the numerical and analytical solutions of temperature ($\psi = T$) or velocity ($\psi = u$). We carry out some simulations at different values of κ_r and present the results in Table I, where a comparison between the present LB method and those in Refs. [56,58] is provided. As seen from this table, all methods can work well for this problem with a large κ_r, but the present LB method is more accurate than that in Ref. [58] and comparable to the one in Ref. [56]. In addition, to see the difference between the analytical and numerical solutions more clearly, we plot the velocity and temperature

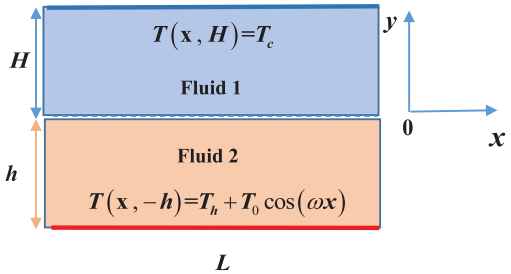

FIG. 6. Schematic of two-phase thermocapillary flow in a nonuniform heated channel.

TABLE I. Relative errors of different LB methods at different ratios of the thermal conductivity (blank entries mean that no result was reported).

κ_r	Err	Present work	Ref. [56]	Ref. [58]
0.1	U_x	5.09×10^{-2}		
0.1	U_y	5.84×10^{-2}		
0.1	T	1.20×10^{-3}		
0.2	U_x	4.91×10^{-2}		
0.2	U_y	5.90×10^{-2}	8.41×10^{-2}	14.18×10^{-2}
0.2	T	6.73×10^{-4}	5.23×10^{-3}	7.65×10^{-3}
1	U_x	4.35×10^{-2}		
1	U_y	5.80×10^{-2}	5.71×10^{-2}	11.83×10^{-2}
1	T	3.06×10^{-4}	2.25×10^{-4}	8.27×10^{-4}

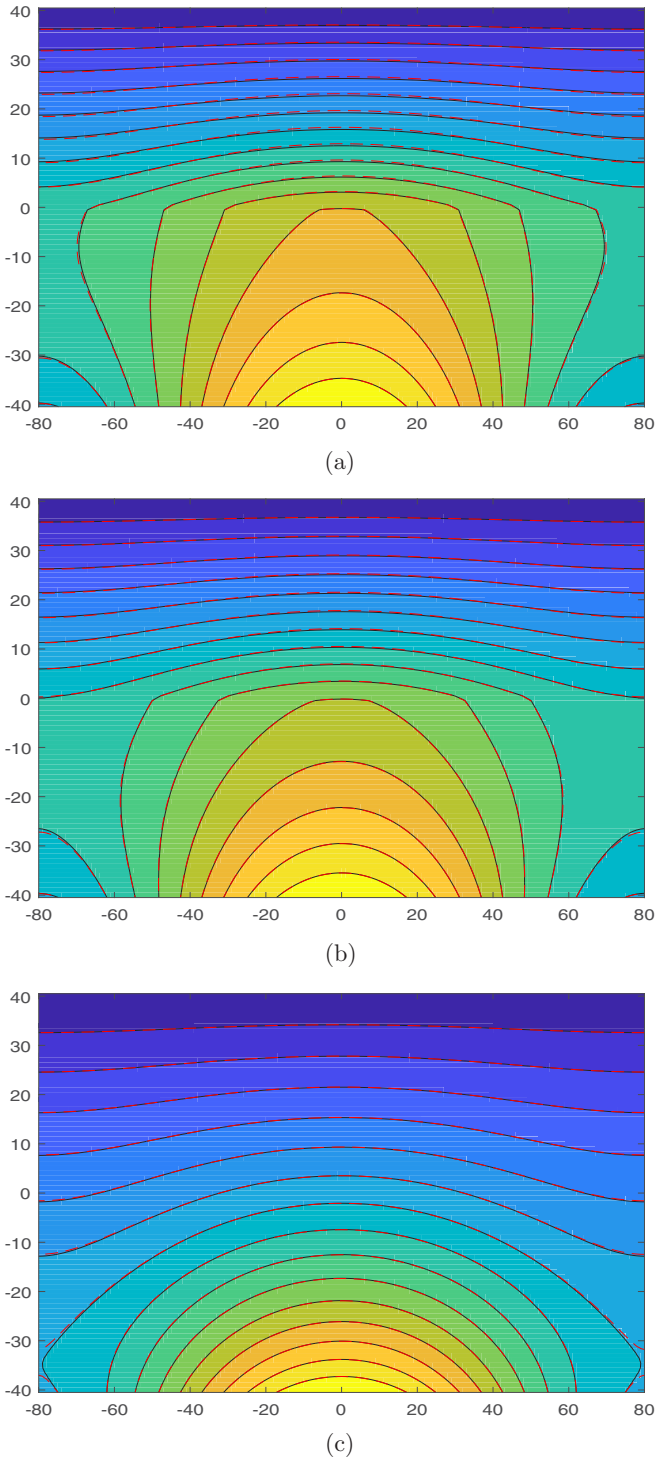

FIG. 7. Contours of temperature at different thermal conductivity ratios (a) $\kappa_r = 0.1$, (b) $\kappa_r = 0.2$, and (c) $\kappa_r = 1$.

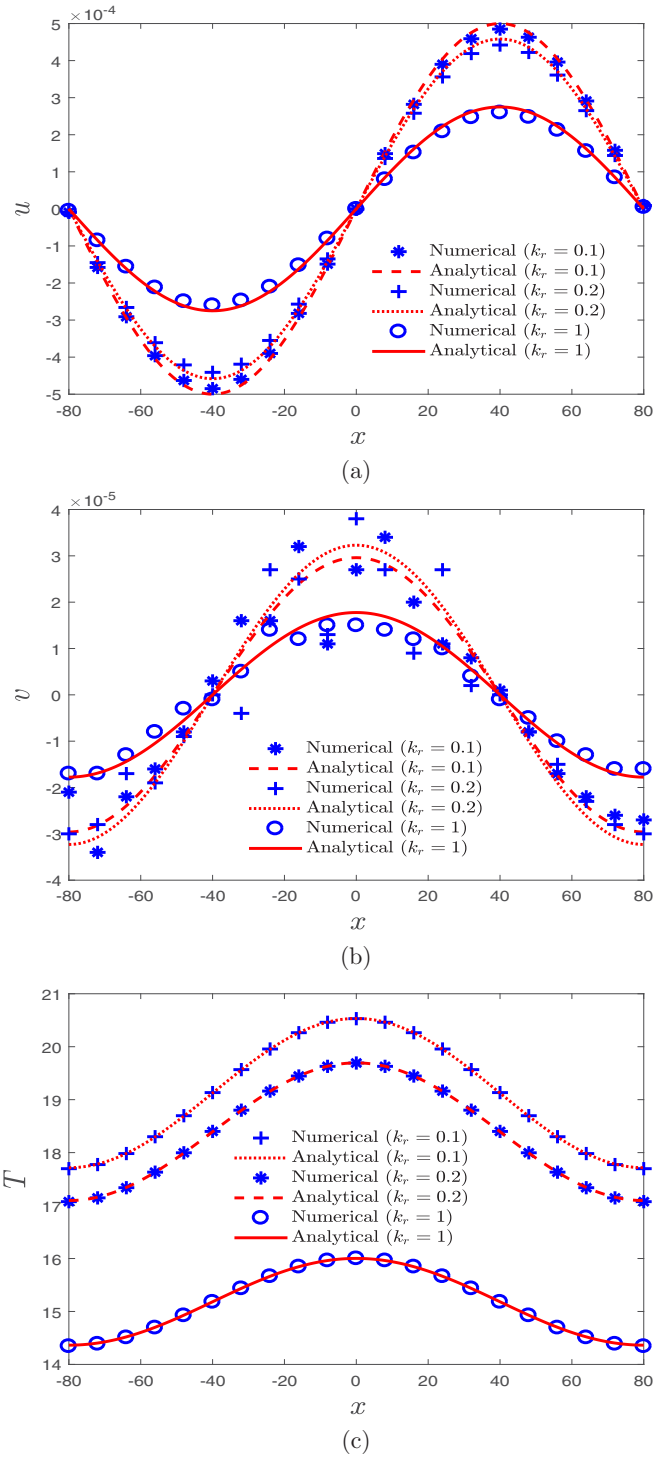

FIG. 8. Profiles of velocity and temperature along the central line of the domain in the x direction at (a) $\kappa_r = 0.1$, (b) $\kappa_r = 0.2$, and (c) $\kappa_r = 1$.

profiles along the central lines in Figs. 8 and 9. From these two figures, one can see that the numerical results are very close to the analytical solutions, while the deviation between the numerical and analytical solutions of velocity becomes large with the decrease of κ_r, which may be caused by the finite thickness of the diffusion interface of the phase-field method. Although the thermal conductivity changes with the diffusion interface, a small κ_r will result in the temperature deviation in the diffusion interface. The difference in the temperature gradient will inevitably affect the surface tension of the interface, which in turn affects the velocity distribution. On the other hand, the analytical solutions of this problem are derived without considering the diffusion interface, which may lead to some differences between the numerical and analytical

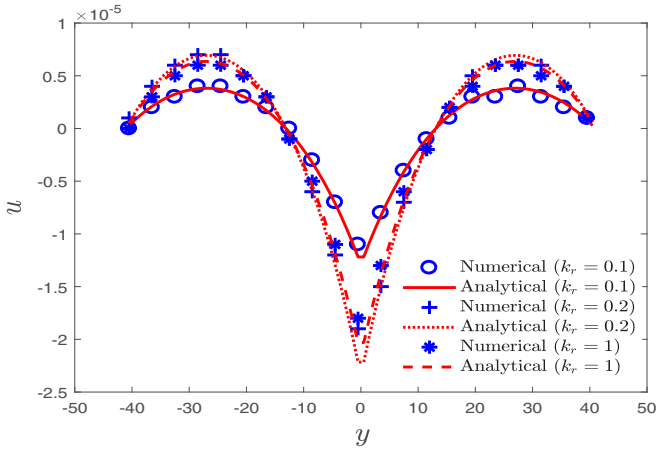

(a)

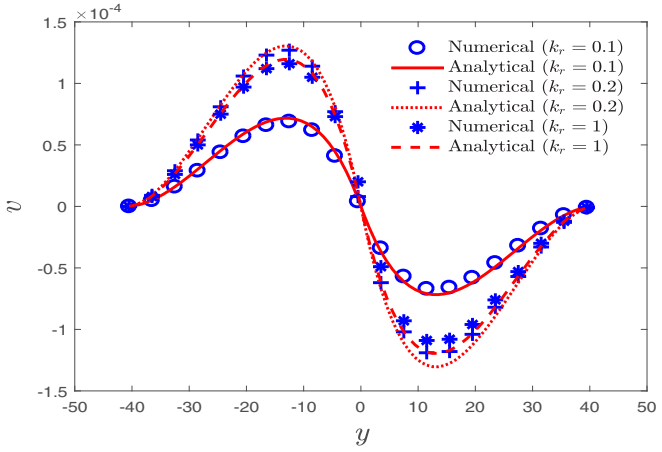

(b)

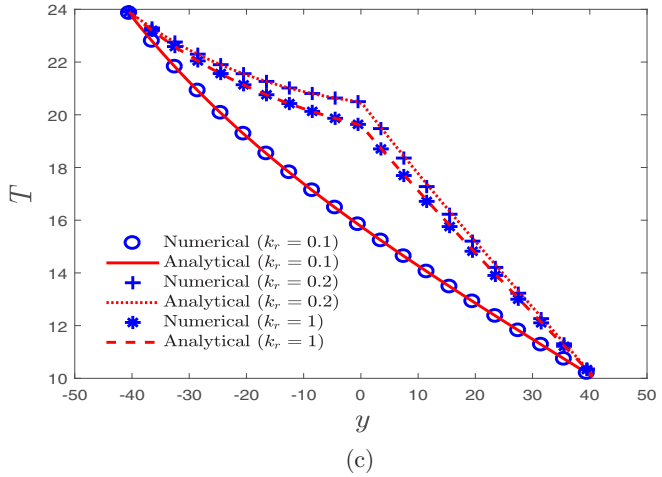

(c)

FIG. 9. Profiles of velocity and temperature along the central line of the domain in the y direction at (a) $\kappa_r = 0.1$, (b) $\kappa_r = 0.2$, and (c) $\kappa_r = 1$.

solutions of velocity. This phenomenon is also observed in some available works [56,59]. Moreover, we also present the contour lines of the y -component of velocity in Fig. 10, where $\kappa_r = 1$, and clearly observe the asymmetry and fluctuations at the interface, but they are not obvious far away from the interface.

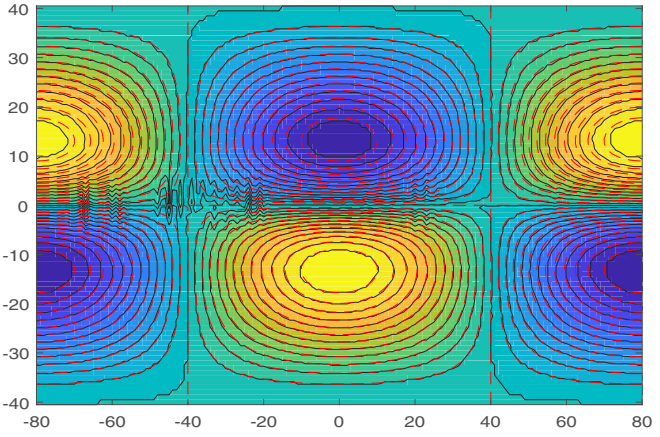

FIG. 10. Contour lines of the y component of velocity.

C. Thermocapillary migration of a deformable bubble

In this section we further consider the thermocapillary migration of a deformable bubble, which is caused by the nonuniform surface tension induced by the temperature gradient imposed at the phase interface. We note that the problem of the thermocapillary migration of a bubble was first studied theoretically by Young *et al.* in [12], in which an expression of the migration velocity known as U_{YGB} velocity was obtained under the condition of small Ma and Re,

$$U_{\mathrm{YGB}} = \frac{2U}{(2+3\mu_r)(2+\kappa_r)}. \tag{60}$$

The characteristic velocity U is defined as

$$U = \frac{\sigma_T \nabla T R}{\mu_2}, \tag{61}$$

where ∇T is a constant temperature gradient and R is the radius of the bubble. As shown in Fig. 11, a bubble with $R =$

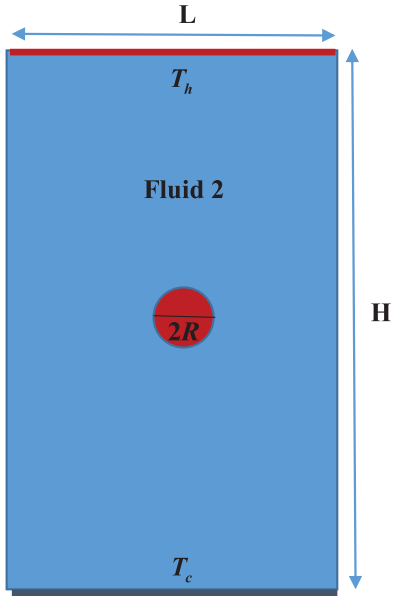

FIG. 11. Schematic of the thermocapillary migration of a deformable bubble in the nonuniform temperature field.

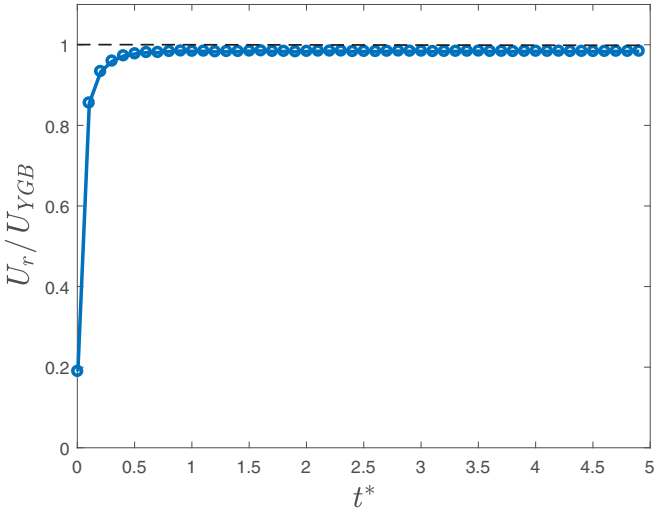

FIG. 12. Time evolution of the normalized migration velocity at Re = 0.1 and Ma = 0.1. The numerical results are denoted by circles and the theoretical results by the dashed line.

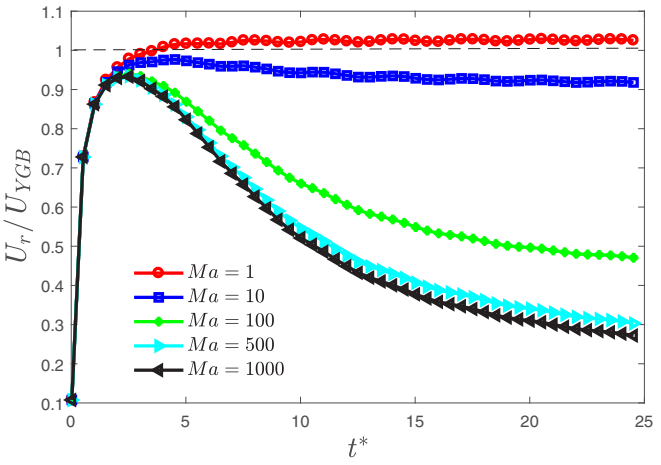

FIG. 13. Time evolution of the normalized migration velocity at different values of Ma. The numerical results are denoted by symbols and the theoretical results by the dashed line.

$20\Delta x$ is initially located at the center of the computational region with a length of $320\Delta x$ and width of $160\Delta x$. On the top and bottom walls, the no-flux boundary condition is used for the phase field, the nonslip condition is applied for the flow field, and the Dirichlet boundary conditions with $T_h = 32$ and $T_c = 16$ are adopted for the temperature field. For the left and right boundaries, the periodic boundary condition is imposed for all fields. During the initialization, the flow field is kept stationary and the temperature field has a linear distribution in the y direction.

The thermocapillary migration of the deformable bubble or droplet has been numerically studied in some previous works [24,25,56,60]. Like the one in Ref. [56], we first consider the simple case with the density ratio $\rho_r = 1$ ($\rho_1 = \rho_2 = 1$), $C_{p_1} = C_{p_2} = 1$, $\nu_1 = \nu_2 = 0.2$, $T_{\text{ref}} = 16$, $\sigma_{\text{ref}} = 2.5 \times 10^{-3}$, $\nabla T = 0.1$, and $\sigma_T = 10^{-4}$ (see Fig. 11). Substituting these values into Eqs. (40), (41), (60), and (61), we can obtain the theoretical value of the migration velocity $U_{\text{YGB}} = 1.33\hat{3} \times 10^{-4}$, Re = Ma = 0.1, and Ca = 0.08. In our simulations, the numerical migration velocity of the droplet or bubble is calculated as

$$U_r(t) = \frac{\int_V \phi u_d dV}{\int_V \phi dV} = \frac{\sum_{\mathbf{x}} \phi(\mathbf{x},t) u_d(\mathbf{x},t)}{\sum_{\mathbf{x}} \phi(\mathbf{x},t)}, \quad \phi < 0, \quad (62)$$

where u_d is the numerical velocity. Figure 12 shows the temporal evolution of the numerical migration velocity normalized by U_{YGB}. From this figure, one can observe that the numerical velocity is in agreement with the analytical prediction [12] and the relative error $E_r = |U_r - U_{\text{YGB}}|/U_{\text{YGB}}$ is about 1.65%, which is much smaller than that reported in Ref. [59].

We continue to investigate thermocapillary migration of a bubble at large Ma where the theoretical expression of the migration velocity would be inaccurate and compare the present results with those in Ref. [56]. In Fig. 13, where Re = 1, Ca = 0.1, $\sigma_T = 2.5 \times 10^{-4}$, $\sigma_{\text{ref}} = 5 \times 10^{-3}$, and $\nu_1 = \nu_2 = 0.1$, we present the evolution of the normalized migration velocity at five different values of Ma (Ma = 1, 10, 100, 500, and 1000), which can be realized through adjusting κ_1 and κ_2. As shown in this figure, the velocity of the bubble first increases to the maximum and finally reaches a constant for all cases under consideration. Also, the migration velocity decreases gradually with the increase of Ma, which agrees with the previous theoretical and numerical studies [56,79–81]. Actually, for the cases with relatively small values of Ma, this phenomenon can be explained by the temperature distribution inside the bubble. From Fig. 14 we can observe that the temperature gradient inside the bubble decreases gradually with the increase of Ma, and a small average temperature gradient will reduce the driving force for the bubble migration. To see this more clearly, we also present the velocity of the bubble in Fig. 14 where the recirculation flow is observed, and the vortex intensity decreases as the Ma increases. However, when Ma is large enough, one can see in Fig. 15 that there are some differences between the present results of the temperature and velocity and some available works [53,81]; this is because the two-dimensional problem considered in this work is not consistent with the three-dimensional one investigated in the previous works [53,81]. Next we focus on the impact of Re on the thermocapillary migration of a droplet. To this end, the values of Re are set as 1, 10, 20, 40, 100, and 200, which are determined by the values of viscosity $\nu = 0.1$ 0.0316, 0.02, 0.0157, 0.01, and 0.0071; the other parameters are the same as those of the case with small Re. Figure 16 shows the normalized migration velocity of the droplet at different values of Re. It is found that as the value of Re increases, the terminal velocity decreases and more time is needed to reach the steady state, which is similar to the previous work [81] at small Re. Also, the present LB method is still effective for the case with large Re.

In addition, to show the capacity of the present LB method in the study of the thermocapillary flows with the high density ratios, we perform some simulations at five different density ratios (ρ_r = 10:1, 50:1, 100:1, 200:1, and 1000:1). In our simulations, $\rho_2 = 1.0$, $\nu_1 = \nu_2 = 0.2$, $\sigma_{\text{ref}} = 2.5 \times 10^{-4}$, $\sigma_T = 10^{-5}$, $\kappa_2 = 0.2$, $C_{p_1} = 2$, and $C_{p_1} = 5$, which can lead to Re = 0.01, Ma = 0.05, and Ca = 20. The interface thickness

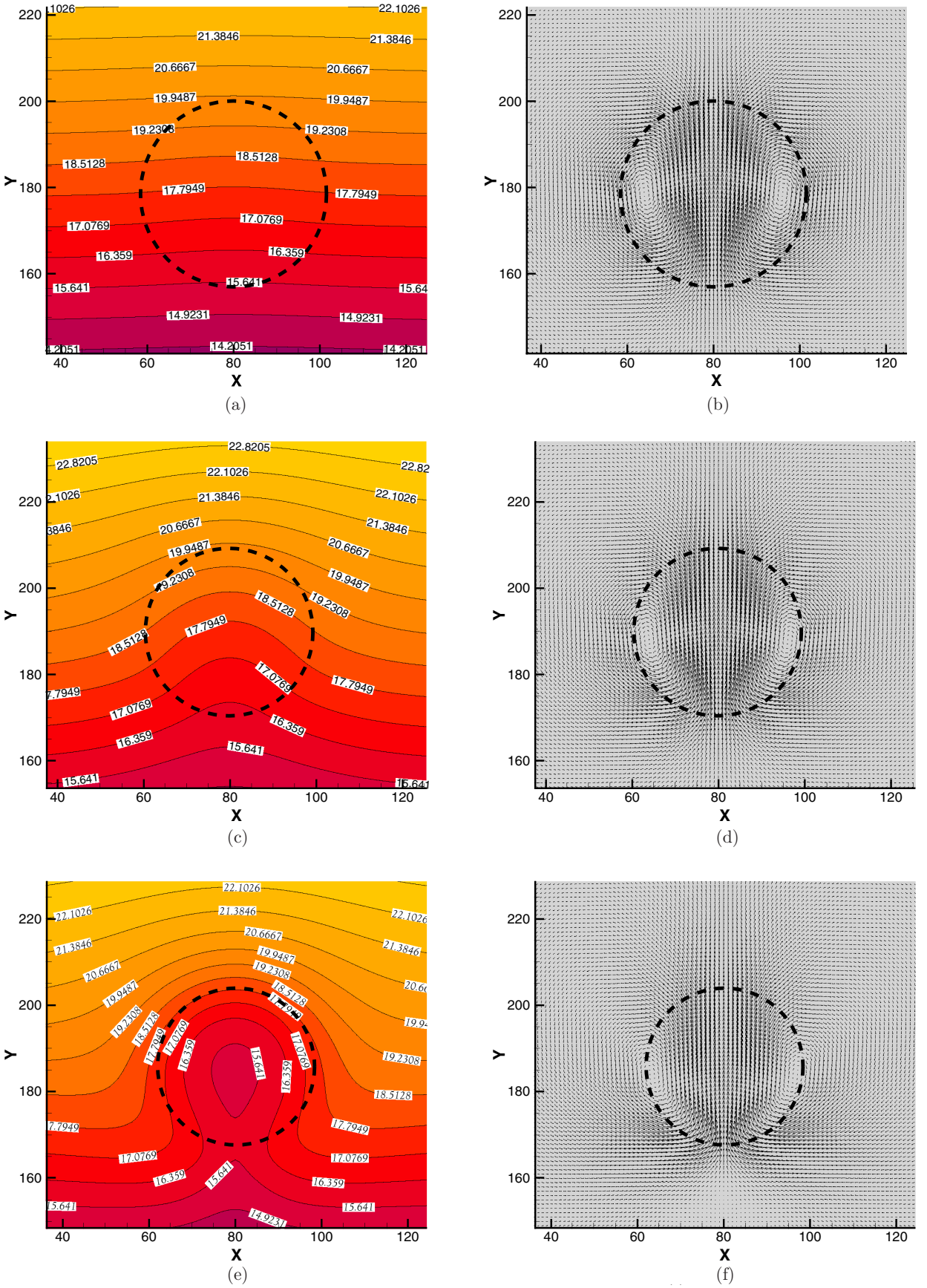

FIG. 14. Distributions of temperature [(a), (c), (e)] and velocity [(b), (d), (f)] around the rising bubble at Ma = 1 [(a), (b)], Ma = 10 [(c), (d)], and Ma = 100 [(e), (f)].

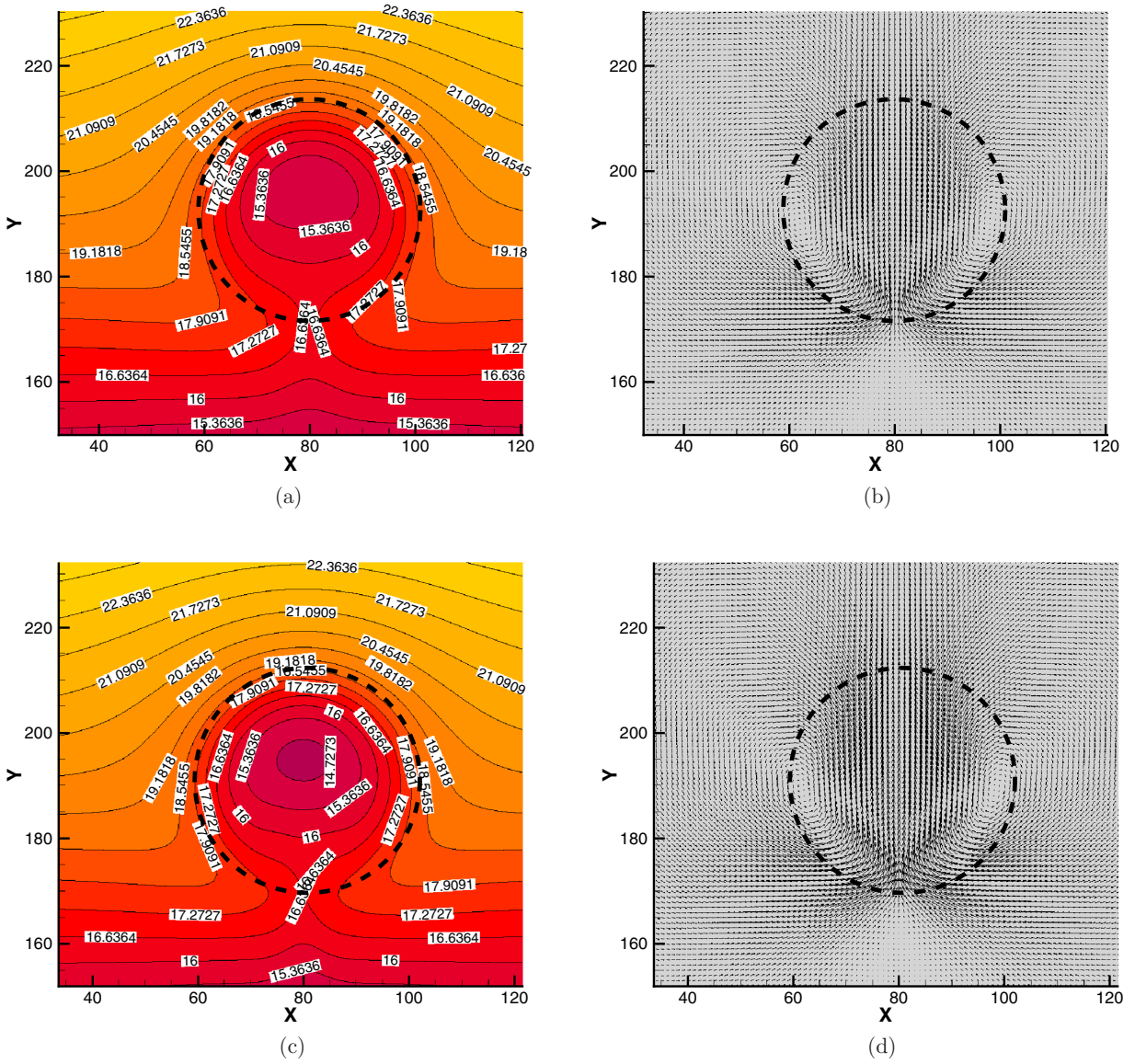

FIG. 15. Distributions of temperature [(a), (c)] and velocity [(b), (d)] around the rising bubble at Ma = 500 [(a), (b)] and Ma = 1000 [(c), (d)].

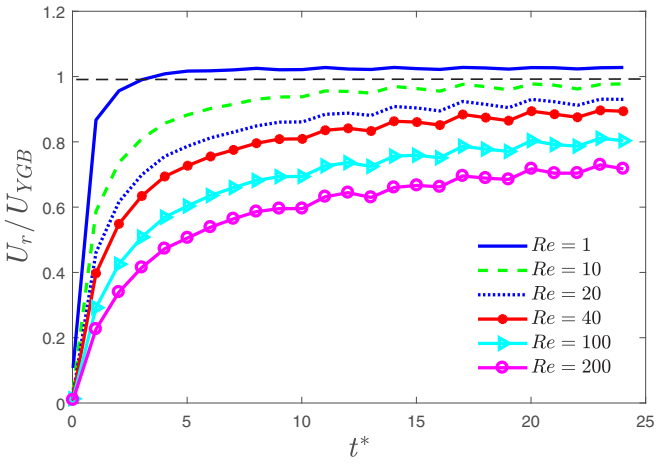

FIG. 16. Time evolution of the normalized migration velocity at Ma = 1 and Re = 1, 10, 20, 40, 100, and 200. The numerical results are denoted by symbols and the theoretical results by the dashed line.

is taken as $D = 3$ and the thermal conductivity of the gas phase can be calculated as $\mathrm{Pr}_1 = \rho_1 C_{p_1} \nu_1 / \kappa_1 = 1$. We present the evolution of the bubble velocity normalized by U_{YGB} in Fig. 17; we also calculated the terminal bubble velocity and list the relative errors in Table II. From Fig. 17 and Table II one can find that the velocity increases with the increase of the density ratio and the present LB method is also accurate for the thermocapillary migration of the bubble, even with a large

TABLE II. Relative errors of migration velocity at different density ratios.

ρ_r	U_{YGB}	Present work	E_r (%)
10	3.9526×10^{-5}	3.8195×10^{-5}	3.37
50	4.7592×10^{-5}	4.8253×10^{-5}	1.39
100	4.8773×10^{-5}	4.9773×10^{-5}	2.05
200	4.9381×10^{-5}	5.0432×10^{-5}	2.13
1000	4.9875×10^{-5}	5.0587×10^{-5}	1.43

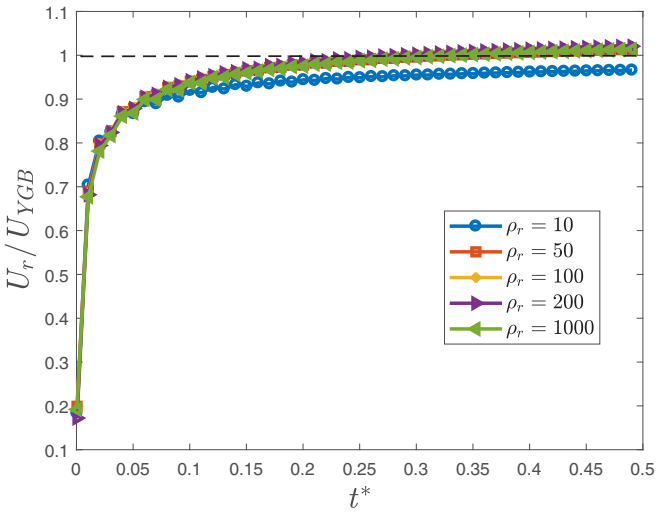

FIG. 17. Time evolution of normalized migration velocity at different density ratios. The numerical results are denoted by symbols and the theoretical results by the dashed line.

density ratio. Further, we plot the velocity and temperature distributions in Fig. 18 and find that the temperature and flow fields at different density ratios are similar, which is also consistent with the previous results [56].

Finally, we also test the present LB method for thermocapillary flows with high viscosity ratios. To this end, we carry out some simulations of the thermocapillary migration of the bubble under four different viscosity ratios (ν_r = 10:1, 20:1, 50:1, and 100:1) and set the other parameters as $\nu_1 = 0.2$, $\rho_1 = \rho_2 = 1$, $\sigma_{\text{ref}} = 2.5 \times 10^{-4}$, $\sigma_T = 10^{-5}$, $C_{p_{1,2}} = 2$, $\kappa_1 = 0.2$, and $\kappa_2 = 0.02$. Through these parameters, we can obtain Re = 0.01, Ma = 0.001, and Ca = 0.08. From the results shown in Fig. 19, one can observe that the velocity of thermocapillary migration first increases rapidly and then gradually tends to be stable with the evolution of time. We also show a comparison of the numerical migration velocity and the theoretical one (U_{YGB}) in Table III. As seen from this table, the present LB method can also give accurate results, even for the case with a large viscosity ratio.

IV. CONCLUSION

In this paper, we proposed an improved lattice Boltzmann method for thermocapillary flows where an effective LB model was developed for the governing equation of the temperature field. To solve the temperature equation more accurately and more efficiently, we first rewrote the convection-diffusion equation of temperature as a diffusion equation in which the convection term is considered as a source term and then developed a simple LB model for the temperature equation. Through the Chapman-Enskog analysis, the macroscopic governing equations of the thermocapillary flows could be recovered correctly from the present LB method. In addition, we also conducted some simulations to test the accuracy of the present LB method and found that the numerical results agree well with analytical solutions and available numerical data. Compared to previous works [59,60], the present LB method is much simpler and more accurate. Furthermore, the present LB method also has the potential in the study of thermocapillary flows with large density, viscosity, and thermal conductivity ratios.

TABLE III. Relative errors of migration velocity at different ratios of the viscosity.

ν_r	U_{YGB}	Present work	E_r (%)
10	4.1408×10^{-5}	4.1799×10^{-5}	0.94
20	4.4297×10^{-5}	4.4363×10^{-5}	0.15
50	4.6232×10^{-5}	4.6186×10^{-5}	0.10
100	4.6915×10^{-5}	4.6899×10^{-5}	0.03

ACKNOWLEDGMENTS

This work was supported by the National Natural Science Foundation of China (Grants No. 12072127, No. 51836003, and No. 11972266), the Graduates' Innovation Fund, Huazhong University of Science and Technology (Grant No. 2020yjsCXCY034), and the Natural Science Foundation of Hubei Province (Grant No. 2020CFB384).

APPENDIX A: CHAPMAN-ENSKOG ANALYSIS OF THE PRESENT LB MODEL FOR THE TEMPERATURE EQUATION

In the Appendix we carry out a detailed Chapman-Enskog analysis to derive the temperature equation from the present LB model. For this purpose, we first expand the distribution function h_k, the source term H_k, and the derivatives of time and space as [38,82]

$$h_k = h_k^{(0)} + \epsilon h_k^{(1)} + \epsilon^2 h_k^{(2)} + \cdots, \tag{A1a}$$

$$H_k = \epsilon H_k^{(1)}, \quad H_k^{(1)} = \omega_k R_1^{(1)}, \tag{A1b}$$

$$\partial_t = \epsilon \partial_t^{(1)} + \epsilon^2 \partial_t^{(2)} + \cdots, \tag{A1c}$$

$$\nabla = \epsilon \nabla_1 + \cdots, \tag{A1d}$$

where ϵ is a small parameter and $R_1^{(1)}$ is given by

$$R_1^{(1)} = -\mathbf{u} \cdot \nabla_1 T - \kappa \nabla_1 T \cdot \left[-\frac{\rho(c_{p_l} - c_{p_g}) + c_p(\rho_l - \rho_g)}{(\rho c_p)^2(\phi_l - \phi_g)} \right] \nabla_1 \phi. \tag{A2}$$

Applying the Taylor expansion to Eq. (35), we can obtain

$$D_k h_k + \frac{\Delta t}{2} D_k^2 h_k = -\frac{1}{\Delta t \tau_h}\left(h_k - h_k^{\text{eq}}\right) + \left(1 - \frac{1}{2\tau_h}\right) H_k, \tag{A3}$$

where $D_k = \partial_t + \mathbf{c}_k \cdot \nabla$. Substituting Eq. (A1) into Eq. (A3) yields

$$\left(\epsilon D_{1k} + \epsilon^2 \partial_{t_2}\right)\left[h_k^{(0)} + \epsilon h_k^{(1)} + \epsilon^2 h_k^{(2)}\right] + \frac{\Delta t}{2}\left(\epsilon D_{1k} + \epsilon^2 \partial_{t_2}\right)^2 \left(h_k^{(0)} + \epsilon h_k^{(1)} + \epsilon^2 h_k^{(2)}\right) = -\frac{1}{\tau_h \Delta t}\left(h_k^{(0)} + \epsilon h_k^{(1)}\right.$$

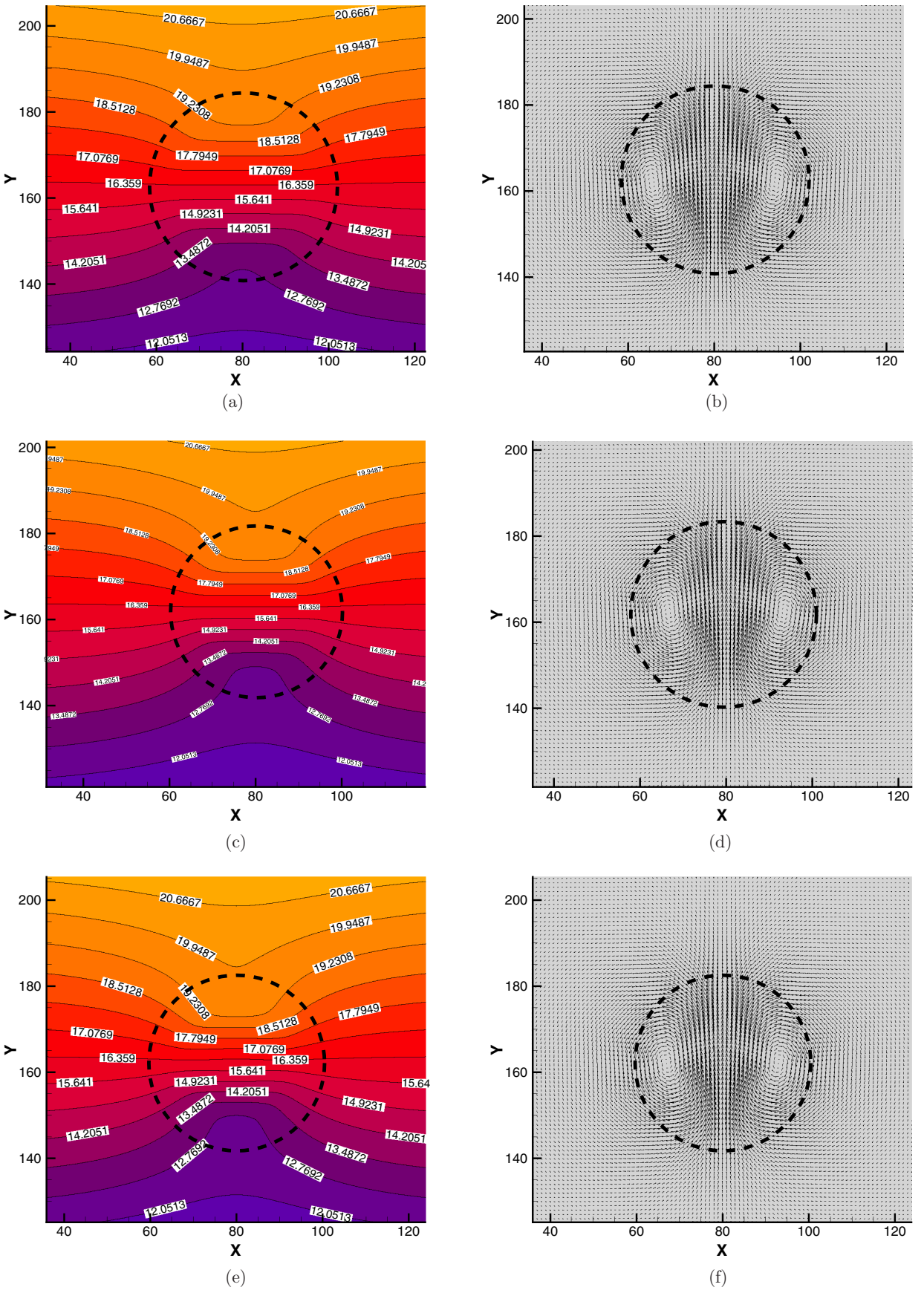

FIG. 18. Distributions of temperature [(a), (c), (e), (g), (i)] and velocity [(b), (d), (f), (h), (j)] at $\rho r = 10$ [(a), (b)], $\rho r = 50$ [(c), (d)], $\rho r = 100$ [(e), (f)].

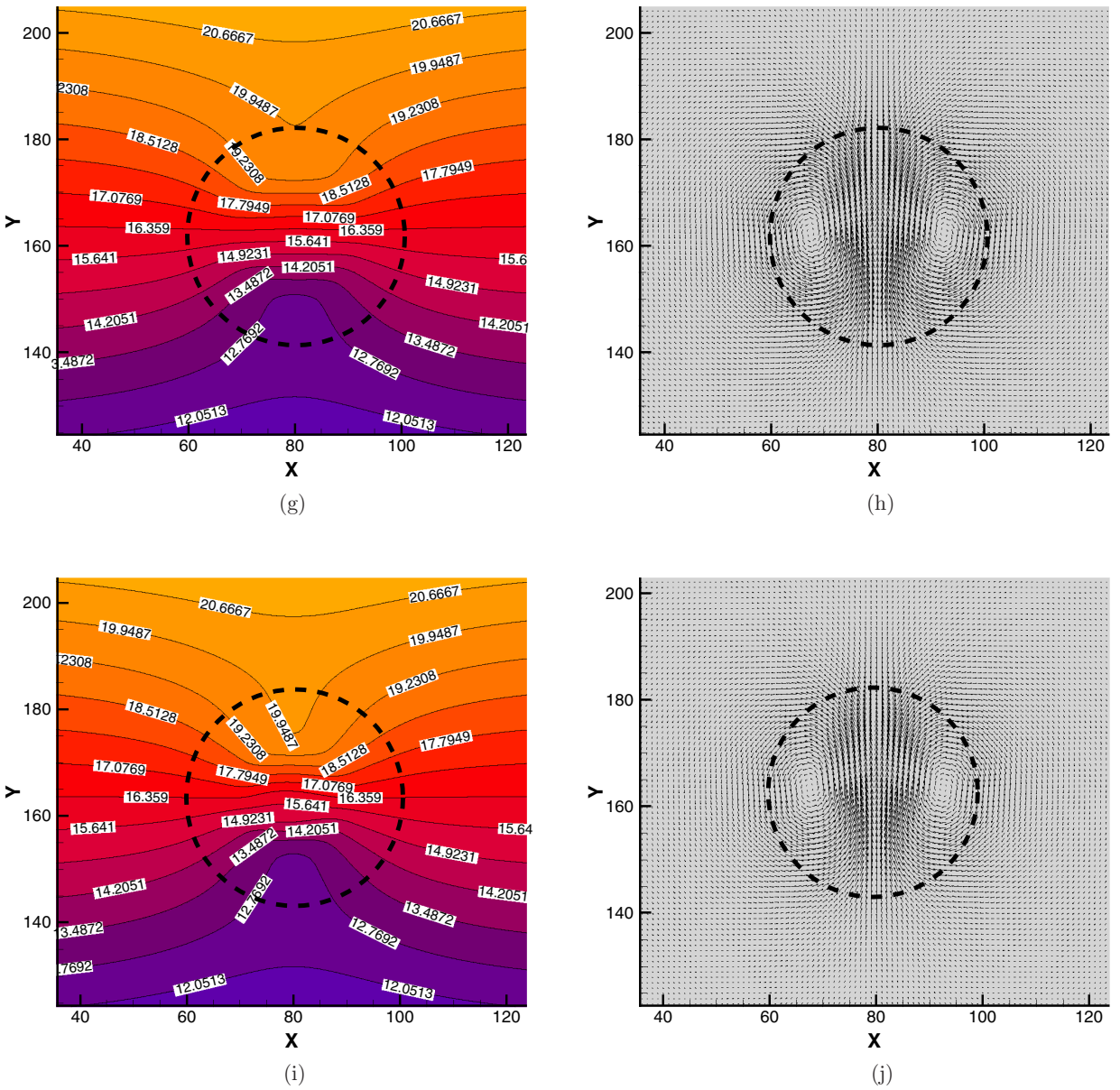

FIG. 18. (*Continued.*) $\rho r = 200$ [(g), (h)], and $\rho r = 1000$ [(i), (j)].

$$+\epsilon^2 h_k^{(2)} - h_k^{\mathrm{eq}}) + \left(1 - \frac{1}{2\tau_h}\right)\epsilon H_k^{(1)}, \tag{A4}$$

where $D_{1k} = \partial_{t_1} + \mathbf{c}_k \cdot \nabla_1$. Based on Eq. (35), we can derive the equations at the orders of ϵ^0, ϵ^1, and ϵ^2, respectively:

$$h_k^{(0)} = h_k^{\mathrm{eq}}, \tag{A5a}$$

$$D_{1k} h_k^{(0)} = -\frac{1}{\tau_h \Delta t} h_k^{(1)} + \left(1 - \frac{1}{2\tau_h}\right) H_k^{(1)}, \tag{A5b}$$

$$\partial_{t_2} h_k^{(0)} + D_{1k} h_k^{(1)} + \frac{\Delta t}{2} D_{1k}^2 h_k^{(0)} = -\frac{1}{\tau_h \Delta t} h_k^{(2)}. \tag{A5c}$$

Substituting Eq. (A5b) into Eq. (A5c), we obtain

$$\partial_{t_2} h_k^{(0)} + D_{1k}\left(1 - \frac{1}{2\tau_h}\right) h_k^{(1)} + \frac{\Delta t}{2} D_{1k}\left(1 - \frac{1}{2\tau_h}\right) H_k^{(1)} = -\frac{1}{\tau_h \Delta t} h_k^{(2)}. \tag{A6}$$

According to Eqs. (37) and (38b), we have

$$\sum_k h_k^{(1)} = -\frac{\Delta t}{2} R_1^{(1)}, \tag{A7}$$

$$\sum_{k=0} h_k^{(i)} = 0, \quad i \geqslant 2. \tag{A8}$$

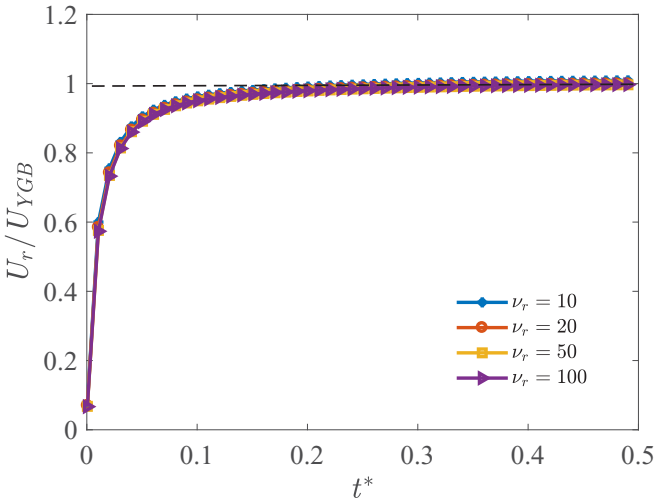

FIG. 19. Time evolution of the migration velocity at different viscosity ratios. The numerical results are denoted by symbols and the theoretical results by the dashed line.

Summing Eqs. (A5c) and (A6) and applying Eqs. (37), (38a), and (38b) gives

$$\partial_{t_1} T = R_1^{(1)}, \tag{A9}$$

$$\partial_{t_2} T + \nabla_1 \left(1 - \frac{1}{2\tau_h}\right) \sum_k \mathbf{c}_k h_k^{(1)} = 0. \tag{A10}$$

In addition, from Eqs. (A5b) and (38) we can obtain

$$\begin{aligned} \sum_k \mathbf{c}_k h_k^{(1)} &= -\tau_h \Delta t \left[\sum_k \mathbf{c}_k D_{1k} h_k^{(0)} - \sum_k \left(1 - \frac{1}{2\tau_h}\right) \mathbf{c}_k H_k^{(1)} \right] \\ &= -\tau_h \Delta t \left(\mathbf{0} + \nabla_1 \cdot \sum_k \mathbf{c}_k \mathbf{c}_k h_k^{(0)} - \mathbf{0} \right) \\ &= -\tau_h \Delta t c_s^2 \nabla_1 T. \end{aligned} \tag{A11}$$

Substituting Eq. (A11) into Eq. (A10), we have

$$\partial_{t_2} T = \nabla_1 \cdot (\alpha \nabla_1 T), \tag{A12}$$

where $\alpha = c_s^2(\tau_h - 0.5)\Delta t$. Combining the equations at t_1 and t_2 scales, i.e., Eqs. (A9) and (A12), we can recover Eq. (29) correctly. In addition, from Eq. (A11) we can also obtain a local scheme for the temperature gradient,

$$\nabla T = -\frac{\sum_k \mathbf{c}_k \left(h_k - h_k^{\mathrm{eq}}\right)}{\tau_h \Delta t c_s^2}. \tag{A13}$$

[1] L. E. Scriven and C. V. Sternling, Nature (London) **187**, 186 (1960).
[2] R. S. Subramanian and R. Balasubramaniam, *The Motion of Bubbles and Drops in Reduced Gravity* (Cambridge University Press, Cambridge, 2001).
[3] K. T. Kotz, K. A. Noble, and G. W. Faris, Appl. Phys. Lett. **85**, 2658 (2004).
[4] A. T. Ohta, A. Jamshidi, J. K. Valley, H.-Y. Hsu, and M. C. Wu, Appl. Phys. Lett. **91**, 074103 (2007).
[5] C. N. Baroud, M. Robert de Saint Vincent, and J.-P. Delville, Lab Chip **7**, 1029 (2007).
[6] C. N. Baroud, J.-P. Delville, F. Gallaire, and R. Wunenburger, Phy. Rev. E **75**, 046302 (2007).
[7] M. Robert de Saint Vincent, R. Wunenburger, and J.-P. Delville, Appl. Phys. Lett. **92**, 154105 (2008).
[8] M. Robert de Saint Vincent and J.-P. Delville, Phys. Rev. E **85**, 026310 (2012).
[9] A. Mohammadtabar, H. Nazaripoor, A. Riad, A. Hemmati, and M. Sadrzadeh, Phys. Fluids **32**, 024106 (2020).
[10] P. H. Hadland, R. Balasubramaniam, G. Wozniak, and R. S. Subramanian, Exp. Fluids **26**, 240 (1999).
[11] Q. Kang, H. L. Cui, L. Hu, and L. Duan, Microgravity Sci. Technol. **20**, 67 (2008).
[12] N. Young, J. Goldstein, and M. Block, J. Fluid Mech. **6**, 350 (1959).
[13] Y. Kamortani and S. Ostrach, J. Heat Transf. **120**, 758 (1998).
[14] Y. Kamortani, S. Ostrach, and J. Masud, J. Fluid Mech. **410**, 211 (2000).
[15] B. Pendse and A. Esmaeeli, Int. J. Therm. Sci. **49**, 1147 (2010).
[16] M. J. Tan, S. G. Bankoff, and S. H. Davis, Phys. Fluids **2**, 313 (1990).
[17] C. Nienhuser and H. Kuhlmann, J. Fluid Mech. **458**, 35 (2002).
[18] C. W. Hirt and B. D. Nichols, J. Comput. Phys. **39**, 201 (1981).
[19] M. Sussman and E. G. Puckett, J. Comput. Phys. **162**, 301 (2000).
[20] S. Ozen, Unverdi, and G. Tryggvason, J. Comput. Phys. **100**, 25 (1992).
[21] G. Tryggvason, B. Bunner, A. Esmaeeli, D. Juric, and N. Al-Rawahi, J. Comput. Phys. **169**, 708 (2001).
[22] S. Mark, S. Peter, and O. Stanley, J. Comput. Phys. **114**, 146 (1994).
[23] M. Sussman, A. S. Almgren, J. B. Bell, P. Colella, L. H. Howell, and M. L. Welcome, J. Comput. Phys. **148**, 81 (1999).
[24] C. Ma and D. Bothe, Int. J. Multiphase Flow **37**, 1045 (2011).
[25] S. Nas and G. Tryggvason, Int. J. Multiphase Flow **29**, 1117 (2003).
[26] M. Lu, J. C. Lu, Y. Zhang, and G. Tryggvason, Phys. Fluids **31**, 062101 (2019).
[27] N. Balcázar, O. Lehmkuhl, J. Rigola, and A. Oliva, Int. J. Multiphase Flow **74**, 125 (2015).
[28] Q. Du and X. B. Feng, in *Handbook of Numerical Analysis*, edited by A. Bonito and R. H. Nochetto (Elsevier, Amsterdam, 2020), Vol. 21, pp. 425–508.
[29] W. Shyy, R. W. Smith, H. S. Udaykumar, and M. M. Rao, *Computational Fluid Dynamics with Moving Boundaries* (Taylor & Francis, Washington, DC, 1996).
[30] R. S. Qin and H. K. Bhadeshia, Mater. Sci. Technol. **26**, 803 (2010).
[31] J. W. Cahn and J. E. Hilliard, J. Chem. Phys. **28**, 258 (1958).

[32] J. W. Cahn and J. E. Hilliard, J. Chem. Phys. **31**, 688 (1959).
[33] S. Allen and J. W. Cahn, Acta Metall. **24**, 425 (1976).
[34] L. Zheng, S. Zheng, and Q. Zhai, Phys. Rev. E **101**, 013305 (2020).
[35] L. Zheng, S. Zheng and Q. Zhai, Phys. Rev. E **101**, 043302 (2020).
[36] Z. Guo and P. Lin, J. Fluid Mech. **766**, 226 (2015).
[37] B. M. Verschueren, F. van de Vosse, and H. E. H. Meijer, J. Fluid Mech. **434**, 153 (2001).
[38] S. Chen and G. D. Doolen, Annu. Rev. Fluid Mech. **30**, 329 (1998).
[39] S. Succi, *The Lattice Boltzmann Equation for Fluid Dynamics and Beyond* (Oxford University Press, Oxford, 2001).
[40] C. K. Aidun and J. R. Clausen, Annu. Rev. Fluid Mech. **42**, 439 (2010).
[41] Q. Kang, P. C. Lichtner, and D. R. Janecky, Adv. Appl. Math. Mech. **2**, 545 (2010).
[42] Z. Chai, H. Liang, R. Du, and B. Shi, SIAM J. Sci. Comput. **41**, B746 (2019).
[43] Z. Guo and C. Shu, *Lattice Boltzmann Method and its Application in Engineering* (World Scientific, Singapore, 2013).
[44] T. Krüger, H. Kusumaatmaja, A. Kuzmin, O. Shardt, G. Silva, and E. M. Viggen, *The Lattice Boltzmann Method Principles and Practice* (Springer International, Cham, 2017).
[45] L. Chen, Q. Kang, Y. Mua, Y.-L. He, and W.-Q. Tao, Int. J. Heat Mass Transf. **76**, 210 (2014).
[46] Y. Zhao, G. G. Pereira, S. Kuang, and B. Shi, Appl. Math. Lett. **114**, 106926 (2021).
[47] A. K. Gunstensen, D. H. Rothman, S. Zaleski, and G. Zanetti, Phys. Rev. A **43**, 4320 (1991).
[48] H. Wang, X. Yuan, H. Liang, Z. Chai, and B. Shi, Capillarity **2**, 33 (2019).
[49] H. L. Wang, Z. H. Chai, B. C. Shi, and H. Liang, Phys. Rev. E **94**, 033304 (2016).
[50] A. Gupta, M. Sbragaglia, D. Belardinelli, and K. Sugiyama, Phys. Rev. E **94**, 063302 (2016).
[51] S. A. Nabavizadeh, M. Eshraghi, and S. D. Felicelli, Appl. Sci. **9**, 57 (2019).
[52] H. Liu, Y. Zhang, and A. J. Valocchi, J. Comput. Phys. **231**, 4433 (2012).
[53] H. Liu, L. Wu, Y. Ba, and G. Xi, Int. J. Heat Mass Transf. **104**, 337 (2017).
[54] H. Liu, A. J. Valocchia, Y.-h. Zhang, and Q. Kang, J. Comput. Phys. **256**, 334 (2014).
[55] H. Liu and Y. Zhang, J. Comput. Phys. **280**, 37 (2015).
[56] H. Liu, A. J. Valocchi, Y. Zhang, and Q. Kang, Phys. Rev. E **87**, 013010 (2013).
[57] T. Lee and L. Liu, J. Comput. Phys. **229**, 8045 (2010).
[58] T. R. Mitchell, M. Majidi, M. H. Rahimian, and C. R. Leonardi, Phys. Fluids **33**, 032108 (2021).
[59] L. Zheng, S. Zheng, and Q. L. Zhai, Phys. Lett. A **380**, 596 (2016).
[60] Y. Hu, De. Li, X. D. Niu and S. Shu, Int. J. Heat Mass Transf. **138**, 809 (2019).
[61] Q. Li and K. H. Luo, Phys. Rev. E **89**, 053022 (2014).
[62] M. Geier, A. Fakhari, and T. H. Lee, Phys. Rev. E **91**, 063309 (2015).
[63] Z. Chai, D. Sun, H. Wang, and B. Shi, Int. J. Heat Mass Transf. **122**, 631 (2018).
[64] H. Liang, J. Xu, J. Chen, H. Wang, Z. Chai, and B. Shi, Phy. Rev. E **97**, 033309 (2018).
[65] B. Shi and Z. Guo, Phys. Rev. E **79**, 016701 (2009).
[66] F. Ren, B. Song, M. C. Sukop, and H. Hu, Phys. Rev. E **94**, 023311 (2016).
[67] Z. Chai, B. Shi, and Z. Guo, J. Sci. Comput. **69**, 355 (2016).
[68] X. Yuan, Z. Chai, H. Wang, and B. Shi, Comput. Math. Appl. **79**, 1759 (2020).
[69] Z. Guo, B. Shi, and N. Wang, J. Comput. Phys. **165**, 288 (2000).
[70] H. Liang, B. C. Shi, Z. L. Guo, and Z. H. Chai, Phys. Rev. E **89**, 053320 (2014).
[71] H. Liang, Z. H. Chai, B. C. Shi, Z. L. Guo, and T. Zhang, Phys. Rev. E **90**, 063311 (2014).
[72] Z. Guo, C. Zheng, and B. Shi, Phys. Rev. E **83**, 036707 (2011).
[73] Y. Zhao, G. G. Pereira, S. Kuang, Z. Chai, and B. Shi, Appl. Math. Lett. **104**, 106250 (2020).
[74] T. Zhang, B. Shi, Z. Guo, Z. Chai, and J. Lu, Phys. Rev. E **85**, 016701 (2012).
[75] I. Ginzburg, Adv. Water Resour. **28**, 1196 (2005).
[76] S. Cui, N. Hong, B. Shi, and Z. Chai, Phys. Rev. E **93**, 043311 (2016).
[77] A. J. C. Ladd, J. Fluid Mech. **271**, 285 (1994).
[78] A. J. C. Ladd, J. Fluid Mech. **271**, 311 (1994).
[79] N. Shankar and R. S. Subramanian, J. Colloid Interface Sci. **123**, 512 (1988).
[80] Y. Wang, X. Lu, L. Zhuang, Z. Tang, and W. Hu, Acta Astronaut. **54**, 325 (2004).
[81] Z. Yin, P. Gao, W. Hu, and L. Chang, Phys. Fluids **20**, 082101 (2008).
[82] Z. Guo, C. Zheng, and B. Shi, Phys. Rev. E **65**, 046308 (2002).